**Showcasing research from Dr Suresh Babu Kalidindi, Department of Chemistry, Central Tribal University of Andhra Pradesh (CTUAP), Andhra Pradesh, India.**

Advancements in porous framework materials for chemiresistive hydrogen sensing: exploring MOFs and COFs

The perspective highlights the recent developments in chemiresistive hydrogen sensing using metal–organic frameworks (MOFs) and covalent organic frameworks (COFs). Additionally, a comparison is drawn between the sensing characteristics of MOFs/COFs and semiconductor materials (SMOs), providing insights into their complementary nature. This article also puts forward synergistic advantages of MOF/COF-SMO hybrids, in overcoming individual material limitations.

## As featured in:



See Suresh Babu Kalidindi *et al.*,
*Dalton Trans.*, 2025, **54**, 3526.

ROYAL SOCIETY
OF **CHEMISTRY**

rsc.li/dalton

## PERSPECTIVE

Check for updates

# Advancements in porous framework materials for chemiresistive hydrogen sensing: exploring MOFs and COFs

Nany Thokala,†[a] Marilyn Esclance DMello,†[b] Krishnaveni Valle,[a] Kiran Vankayala [iD][c] and Suresh Babu Kalidindi [iD] *[d]

Hydrogen is a zero-emissive fuel and has immense potential to replace carbon-emitting fuels in the future. The development of efficient $H_2$ sensors is essential for preventing hazardous situations and facilitating the widespread usage of hydrogen. Chemiresistors are popular gas sensors owing to their attractive properties such as fast response, miniaturization, simple integration with electronics and low cost. Traditionally, semiconducting metal oxides (SMOs) and Pd-based materials have been widely investigated for chemiresistive $H_2$ sensing applications. However, issues such as limited selectivity and poor reliability still hinder their use in real-time applications. Recent advancements have explored metal–organic frameworks (MOFs) and covalent organic frameworks (COFs), offering new perspectives and potential applications in this field. MOFs and COFs belong to the crystalline framework (CF) family of materials and are highly porous, designable materials with tunable pore surfaces featuring sites for $H_2$ interactions. They exhibit good selectivity towards $H_2$ with quick response/recovery times at relatively low temperatures compared to SMOs. Furthermore, they provide an additional advantage of sensing $H_2$ in the absence of oxygen, even at high concentrations of $H_2$. In this perspective article, we summarize recent advancements and challenges in the development of $H_2$ sensors employing MOFs, COFs, and their hybrid composites as sensing elements. Additionally, we discuss our perspective on hybridizing MOFs/COFs with SMOs and other nanomaterials for the future development of advanced $H_2$ sensors.

## 1. Introduction

In recent times, there have been significant advancements in the use of hydrogen as an efficient alternative source of energy. Often regarded as a fuel of the future, hydrogen ($H_2$) is considered to be a key player in significantly overhauling the present energy challenges and global economy.[1–4] The $H_2$ economy envisions a clean and eco-friendly energy system with net zero emission and subsequent reduction in carbon footprints.[5–7] $H_2$ has a high energy content per unit mass (142 kJ $g^{-1}$, about three times that of gasoline) and very low density (0.0899 kg $m^{-3}$), which makes it 1/14 times lighter than air.[8,9] Upon combustion, $H_2$ yields only water and heat energy, and thus, it is free from polluting emissions. This aspect of net zero $CO_2$ emission has attracted attention from researchers around the world to harness its potential for generating electricity and as a transportation fuel.[10] However, commercializing $H_2$ entails inherent risks associated with its explosive and flammable nature, given its wide flammable range of 4.1 to 75% v/v $H_2$ and rapid diffusivity (0.756 $cm^2$ $s^{-1}$), which readily forms a flammable mixture with air.[11,12] Any unexpected leakage of $H_2$ into the air could be catastrophic.[13–15] $H_2$ gas is devoid of colour, odour, and taste. It is totally imperceptible to humans. Inhaling high concentrations of $H_2$ may lead to asphyxiation and could be fatal.[16] Therefore, it is imperative to deploy efficient $H_2$ sensors as safety measures to check for leakages in $H_2$-related energy systems. A meaningful impact of $H_2$ energy can be achieved by implementing safety codes including sensors.

In recent years, chemiresistors have become popular gas sensors and are in demand for detecting gases at trace levels. The chemiresistive technique is an interesting approach due to its attractive features such as straightforward design, ease of processing, cost-effectiveness, and suitability for making small, portable sensing devices.[17,18] Indeed, advancements in the chemiresistive technique have gone beyond those anticipated since T. Seiyama introduced a resistance-based gas

*a Department of Chemistry, Andhra University, Visakhapatnam, 530003, India*
*b Centre for Nano and Soft Matter Sciences, Bengaluru, 562162, India*
*c Department of Chemistry, Birla Institute of Technology and Science (BITS), Pilani, K. K. Birla Goa campus, Goa, 403726, India*
*d Department of Chemistry, Central Tribal University of Andhra Pradesh (CTUAP), Andhra Pradesh, 535003, India. E-mail: ksureshu@gmail.com, suresh.babu@ctuap.ac.in*

† These authors contributed equally.

sensor using zinc oxide (ZnO) thin films in 1962.[19] The work was inspired by the findings of B. W. H. Brattain (1952) and G. Heiland (1954), which revealed the distinctive behaviour of semiconducting materials (Ge) and semiconducting metal oxides (SMOs) such as ZnO in exhibiting variations in conduction properties upon exposure to different gases present in the surrounding atmosphere.[20,21] The first commercial chemiresistive gas sensor based on tin oxide ($SnO_2$) was developed by Taguchi in 1972 for detecting reducing gases.[22,23] Essentially, chemiresistivity is a characteristic of certain materials wherein the intrinsic electrical resistance changes in response to the presence of specific chemical species (gases, vapors) in the surrounding environment. This phenomenon is the basis for chemiresistive sensors that exploit this property to detect and quantify specific gases.[24] The construction of a typical conventional chemiresistive gas sensor includes systematically arranged components such as a heater (for thermal activation), a substrate that integrates electrodes, and the sensing material, as illustrated in Fig. 1. A sensing element/material in a chemiresistive sensor plays a crucial role in dictating sensitivity and selectivity. In this regard, SMOs have been explored widely in chemiresistive gas sensors for sensing various gases including $H_2$.[25] The detection of $H_2$ using SMOs largely depends on the change in electrical resistance when electrons ($e^-$) from the generated surface oxygen species ($O_2^-$, $O^-$ and $O^{2-}$) interact with the $H_2$ gas.[26] The nature of these oxygen species is usually governed by two major factors, operating/sensing temperature (200 °C to 500 °C) and background gas, *i.e.* synthetic air. In the absence of either of these two factors, the detection of gases by SMOs is negligible. The limitations of SMOs can be listed as (i) high operating temperatures, (ii) the lack of selectivity of a target analyte among multiple gases, (iii) saturation of the signal at higher concentrations of the analyte, and (iv) a high consumption of power.[27] Furthermore, limitations of low surface reactivity and sensing kinetics, especially at room temperature, must be addressed.[28] On the other hand, carbon-based materials like carbon nano-
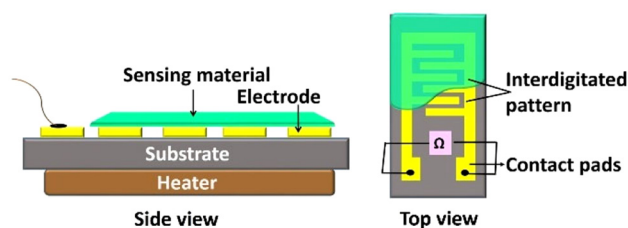


**Fig. 1** Schematic representation of a chemiresistive device. Chemiresistive sensing device (side and top views) with coated sensing material; the device also shows the presence of an interdigitated pattern of electrodes with contact pads to connect the probes to establish suitable contacts to measure the change in resistance of the sensing material. This figure has been reproduced from ref. 17 with permission from IOP, copyright@2021.

tubes (CNTs), graphene, its derivatives [graphene oxide (GO), reduced graphene oxide (rGO)] and conducting polymers have been explored for $H_2$ sensing but with less success.[29–31]

Palladium (Pd) is renowned for its high affinity towards $H_2$, which explains its frequent use in $H_2$-based chemiresistive sensors. The formation of $PdH_x$ (palladium hydride) during $H_2$ sensing is one of the most widely accepted mechanisms for Pd-based sensors.[32,33] Pd exhibits high selectivity for chemisorbed $H_2$ and is capable of dissociating $H_2$ and hosting the H species in its interstitial lattice sites through the formation of $PdH_x$. Initially, a solid solution known as the α-phase (α-$PdH_x$) is formed. As the $H_2$ concentration increases, a transition from the α-phase to the more stable β-phase (β-$PdH_x$) occurs. Eventually, a two-phase equilibrium is achieved, where both α and β phases coexist. The phase transition from α to β is accompanied by volume expansion and lattice strain, which causes changes in electrical resistivity and corresponding changes in output signals.[34] These changes can be effectively achieved under ambient conditions, which is why Pd is a highly preferred sensor element for $H_2$ sensors. However, the formation of an irreversible β-phase may introduce hysteresis,

*Dr Nany Thokala, received her Master's degree in Chemistry from Andhra University, Visakhapatnam, India. She completed her Ph.D. at the same university, in 2023. Her area of research focuses on designing COFs and other related organic materials for application in chemical sensors.*

**Nany Thokala**

*Dr Marilyn Esclance DMello is currently a national postdoctoral fellow (N-PDF, SERB) at the Centre for Nano and Soft Matter Sciences (CeNS), Bangalore, India. She completed her Ph.D. at the Poornaprajna Institute of Scientific Research (PPISR), Bangalore, affiliated to the Manipal Academy of Higher Education (MAHE), Manipal, India, in 2022. Her research interests include the development of porous materials (MOFs/COFs) for application in energy storage, catalysis and gas sensors.*

**Marilyn Esclance DMello**

resulting in a poor response, slow recovery, and poor stability of the sensor with inaccurate electrical read-outs.[35] These issues can be addressed by modifying the Pd surface (the first contact with $H_2$) or by selecting a substrate material with a large surface area and robust structure, capable of withstanding mechanical stress.[36]

With the pressing need for reliable and cost-effective sensors, alternative materials characterized by a large surface area and tuneable porosity are sought for improving the sensing performance.[37–39] Amidst the debate, metal–organic frameworks (MOFs) and covalent–organic frameworks (COFs) are thriving materials from the family of crystalline frameworks (CFs) with inherent features of a high degree of porosity and large surface area, and thus, have immense potential to be utilized as sensor elements for chemiresistive $H_2$ sensors.[40] In this review, CFs specifically refer to MOFs and COFs. The unique characteristics of CFs include (a) ultrahigh porosity, (b) large surface area, (c) tailorable pore sizes/volume, (d) flexibility in modifying the internal surface area, and (e) good thermal/chemical stability.[41] It is worth noting that the linkers can be rationally selected in the design of MOFs and COFs as they influence the MOF/COF–$H_2$ interactions. MOFs possess topological diversity and are synthesized using different metal ions/nodes coordinated to many different organic linkers. Often transition metal ions are employed and can generally dictate the stability of MOFs based on the coordinative bond strength.[42] Carboxylate based linkers [e.g. benzene-1,4-dicarboxylate ($C_8H_6O_4$/$H_2$BDC)] and nitrogen containing linkers (e.g. imidazoles) have been widely employed for MOF construction. Common examples of MOFs constructed using various metal ions/secondary building units (SBUs) and organic linkers are given in Fig. 2. Further functionalization of these linkers with –OH, –$NH_2$, etc. have aided in regulating the pore chemistry at the atomic level.[44] COFs are regarded as the organic counterparts to MOFs. However, they differ from MOFs by being rich in functionalities. They are exclusively constructed with dynamic covalent bonds and possess a low density.[45–47] Notably, COFs are characterized by uninterrupted planar π-electron delocalisation due to extended π–π conjugations across the two-dimensional (2D) or three-dimensional (3D) structures.[54–56] Some common examples of COFs constructed using organic linkers are represented in Fig. 3.[48]

In general, CFs have been majorly studied for gas storage and gas separation applications since their discovery due to their high surface area and tuneable porosity/pore size.[75] At the same time, they have been overlooked for gas sensing applications, mostly due to their poor electrical conductivity or high electrical resistance. With an increasing understanding of the nature of electrical transport in these classes of materials and advancements in preparing conducting CFs, significant interest has emerged in the domain of chemiresistive sensors fashioned out of CFs. Typically, there are two pathways known to administer charge conduction in CFs: (a) through-bond and (b) through-space.[49,50] "Through-bond" charge transport occurs via direct covalent or coordination bonds between metal ions and organic ligands. "Through-space" conduction occurs via non-covalent interactions, such as π–π stacking or other close spatial arrangements of electroactive components, allowing charges to move between sites that are not directly bonded but are in proximity. Charge propagation may occur through continuous energy bands or may hop/"jump" from one localized site to another via linkers or guests, as illustrated in Fig. 4.

Hopping transport is more prevalent in MOFs, wherein the charges move between localized sites through a hopping electron transfer route across the metal nodes. The generated charges are activated via thermal/photoexcitation or chemical doping routes.[51–54] Predominantly, through-space charge transfer is observed in 2D electrically conductive MOFs. COFs tend to favour both through-bond and through-space charge

**Valle Krishnaveni**

*Valle Krishnaveni is a doctoral research student in the Department of Chemistry at Andhra University, Visakhapatnam, India. She received her Master's degree in Chemistry from the same university previously. Her research focuses on the design and development of MOF/COF-based materials for the chemiresistive sensing of $H_2$ gas and catalysis applications.*

**Kiran Vankayala**

*Dr Kiran Vankayala obtained his Ph.D. degree from the Indian Institute of Science (IISc), Bengaluru, India, in 2013 under the supervision of Prof. S. Sampath. After postdoctoral studies at the Weizmann Institute of Science, Israel, with Prof. Ron Naaman (2014–17) and at University College London (UCL), UK, with Prof. Junwang Tang (2018–19), he joined the Department of Chemistry, Birla Institute of Technology and Science (BITS) Pilani, K. K. Birla Goa campus, Goa, as Assistant Professor in 2019. His research interests focus on the development of functional materials and systems for energy-efficient green hydrogen production.*

transduction.[55–58] The in-plane conjugation within an individual 2D COF layer offers a bond channel with an overall in-plane delocalization of electrons (bond transfer). Whereas, the space charge transfer is constructed through the inter-planar π–π stacking layers in the structure. Electroactive CFs have been in the limelight in recent times, wherein redox-active conjugated functional building blocks can serve as mobile charge carriers. Notably, together, through-bond and hopping charge transfer cannot contribute to the conductivity in CFs as they generate different channels for conductivity.[55] Overall, since the motion of generated charge within the framework critically determines the charge transport performance, a judicious choice of building units, redox-active guests/building blocks, mixed-valence systems, strong π–π stacking, or π-conjugation, and long-range crystallinity are essential in the CF's structure.[59]

M. G. Campbell *et al.* synthesized an electrically conductive 2D MOF, $Cu_3(HITP)_2$ (HITP = 2,3,6,7,10,11-hexaiminotriphenylene), with a hexagonal structure and a slipped-parallel stacking of the 2D sheets.[60] At room temperature, $Cu_3(HITP)_2$ displayed a bulk electrical conductivity of 0.2 S cm$^{-1}$, as measured using the two-probe method. The authors measured the electrical conductivity of $Cu_3(HITP)_2$ by pressing the MOF powder into a pellet. This work represented the first study of using a conductive 2D MOF for a chemiresistive sensing application. $Cu_3(HITP)_2$ was active for sensing ammonia (≤5 ppm, concentration) at room temperature. Moreover, significant studies carried out by E. X. Chen *et al.* using a zeolitic imidazolate framework (ZIF), especially ZIF-67 for sensing formaldehyde and trimethylamine, were among the first studies reported for MOF-based chemiresistive sensor applications.[61] Simultaneously, L. M. Tao *et al.* reported covalent triazine frameworks (CTFs) for the detection of ammonia at room temperature.[62] In another study, using the aromatic annulation of 2,3,9,10,16,17,23,24-octa-aminophthalocyanine nickel (II) and pyrene-4,5,9,10-tetraone, K. A. Mirica's group synthesized COF-DC-8 for the chemiresistive sensing of NH₃, H₂S,
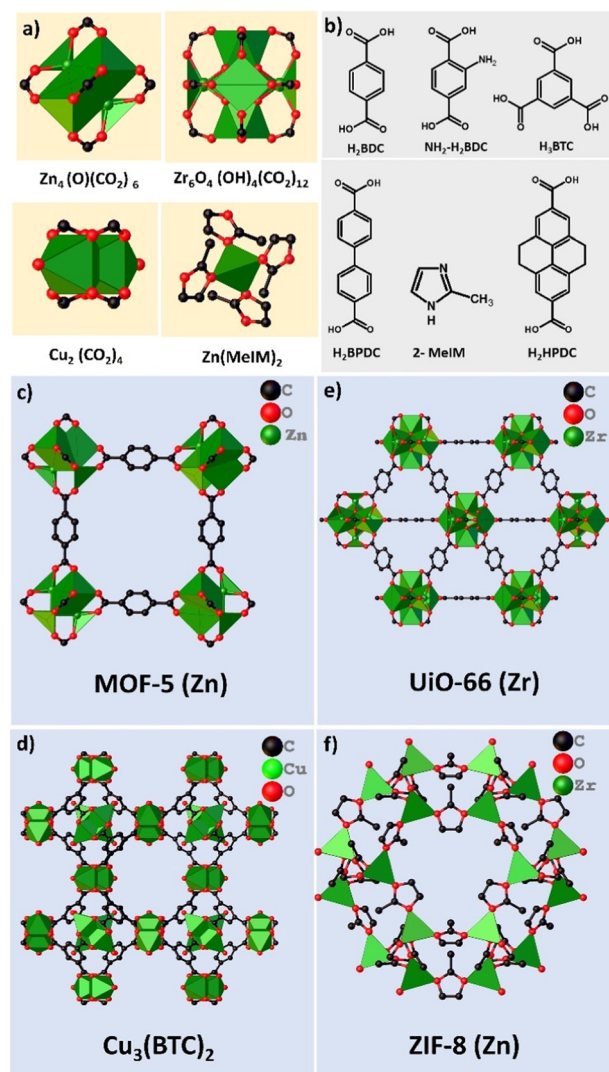


**Fig. 2** Representative examples of (a) secondary building units (SBUs), (b) organic linkers and structures of (c) MOF-5, (d) $Cu_3(BTC)_2$, (e) UiO-66 and (f) ZIF-8 MOFs. This figure has been adapted from ref. 43 with permission from Shodhganga, copyright@2022.

*Dr Suresh Babu Kalidindi obtained his Ph.D. from the Indian Institute of Science (IISc), Bangalore, India, in 2010. He conducted his postdoctoral research at Ruhr University, Germany, and the University of Liverpool, UK. He is a recipient of an Alexander Humboldt fellowship and DST-INSPIRE faculty fellowship. He is currently Associate Professor at the Central Tribal University of Andhra Pradesh, India. His group's research is focussed on hydrogen energy, gas sensors and catalysis.*

**Suresh Babu Kalidindi**

NO, and NO₂ at ppb levels.[63] Since then, many reports on chemiresistive sensing using CFs have been published by various groups, giving insights highlighting the importance of these materials.[64–74,76–78] However, the existing literature lacks a thorough exploration of CFs in the context of developing chemiresistive H₂ sensors. Therefore, this review focuses on the progress made in H₂ sensing utilizing CFs and examines their potential for future applications.

Unlike gases such as NH₃, SO₂, *etc.*, H₂ is a non-polar molecule and as a result, its interactions with the surface of CFs are largely governed by weak van der Waals interactions.[79,80] In a few MOFs, sites like metal nodes and functional groups of linkers do adsorb H₂ reasonably strongly enough to change the resistance of the material. The hybridization of MOFs with SMOs and with Pd NPs is found to be an effective strategy for realizing synergetic H₂ sensing properties.[36,64] The well-
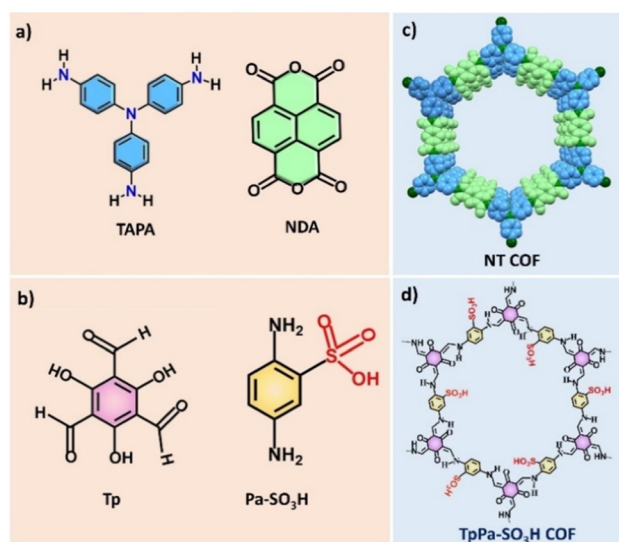
**Fig. 3** Representative examples of organic linkers and structures of COFs; (a), (b) common organic linkers used for COF synthesis; and structures of (c) NT COF and (d) TpPa-SO₃H COF.
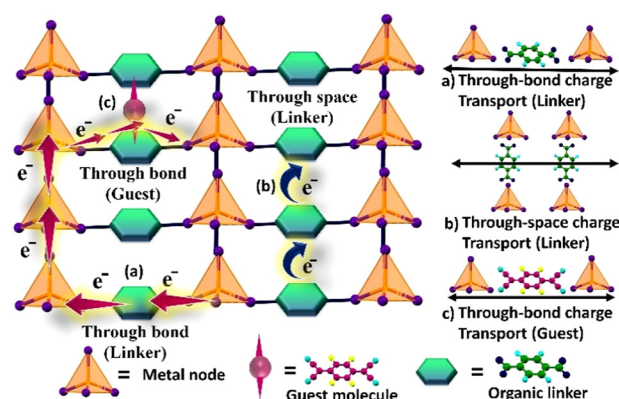


**Fig. 4** Two main charge transport regimes in MOFs: (a) through bond charge transfer *via* linker (band transport); (b) through space charge transfer *via* linker (hopping transport) and (c) through bond charge transfer *via* guest. Reproduced with modifications from ref. 82 from Wiley, copyright@2016.

defined porosity of MOFs is exploited for the sieving of gas molecules by preparing metal oxide@MOF core–shell materials, thereby enhancing the selectivity of metal oxides.[64] Furthermore, nanomaterials derived from MOFs are also actively pursued in order to realize effective H₂ sensors. COFs are generally enriched with a variety of functional groups and contain extended π–π conjugations within the plane. The functional groups are potential sites for interactions with H₂ *via* dipole–induced-dipole interactions and the extended π–π conjugation facilitates the conversion of interactions across the material into a readable signal.[63,81] The versatility of COFs can be further enhanced by hybridizing COFs with H₂-active metal nanoparticles (MNPs) such as Pd, Pt *etc*. This aspect enables

one to utilize the sensing ability of COFs rather than utilizing them as mere supports to stabilize the nanoparticles.

This perspective article initially includes a short discussion on chemiresistive sensing measurements, and the parameters commonly measured/calculated for gas sensing studies (section 2). The article mainly encompasses the latest advancements in the application of porous CFs for chemiresistive H₂ sensing (Scheme 1), section 3, wherein, the H₂ gas sensors are classified as two types: MOFs and COFs. We begin with an overview of MOFs in section 3.1, covering discussions on pristine MOFs, followed by MOF hybrids (MOF-coated SMOs and metal NP-loaded MOFs), and MOF derivatives that are used for chemiresistive H₂ sensing. The latest advancements in COFs for H₂ sensing are discussed in section 3.2. Section 4 offers a comparative discussion on the H₂ sensing mechanisms in SMOs and porous CFs. Finally, in section 5, we present our perspectives on opportunities for developing advanced sensing elements based on CF hybrids, with a focus on integrating MOFs/COFs with SMOs. It is anticipated that this unique structure combines the strengths offered by both of these materials (MOF/COFs and SMOs) while mitigating their inherent drawbacks.

## 2. Chemiresistive sensing measurements

### 2.1 Resistance measurements

The resistance ($R$) of a material can be measured by applying a current ($I$) and measuring the resulting potential ($V$), following Ohm's Law, $V = R \times I$, where $V$ is voltage and $I$ is current. Common approaches to measure resistance include (i) the four-probe method, suitable for a wide range of materials possessing low resistivity including bulk materials, (ii) the two-
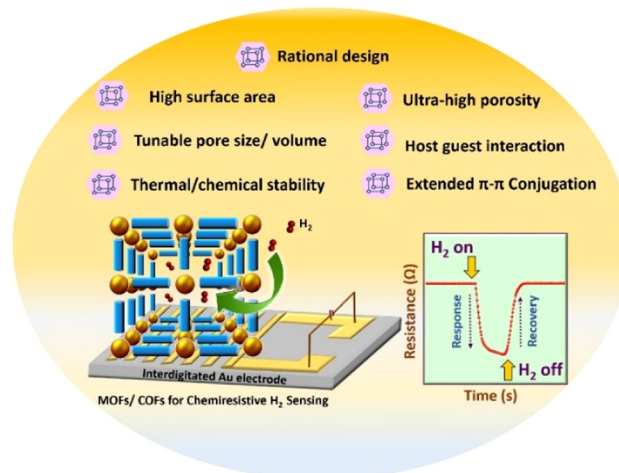


**Scheme 1** Schematic representation of the advantages of MOFs/COFs (CFs) for chemiresistive H₂ sensing. Inset displays the resistance *vs.* time plot for chemiresistive H₂ sensing measurements.

probe method, generally used for materials with high resistivity, (iii) the four-point method (distinct from the four-probe method), and (iv) the van der Pauw method, particularly suitable for measuring very thin films and narrow samples where a set of contacts arranged in a particular geometric pattern are used to calculate the resistivity of the material more accurately.[82,83] The two-probe method is particularly convenient for samples with high resistivity that cannot be measured using the four-probe method.[84,85] This method involves two wires or contact needles (tips) typically made of tempered metal wires (Cu, Pt, W, or Au). These wires make contacts with the samples either using conductive adhesives made with Au, Ag, or graphitic pastes, or by attaching the wires to metal pads through soldering or wire bonding. Interdigitated electrodes (IDEs), patterned on aluminum (Al), silica, glass, or other materials, are suitable devices for two-probe measurements and are the most widely used architectures in chemiresistive sensing devices. Deposition of the sample is typically done either by drop casting the sample dispersed in a suitable solvent or by spraying or applying a slurry of the material on the IDEs. In the case of powdered samples, resistance is usually measured by making the powders into pressed pellets. The contacts on pressed pellets are established by applying adhesive conductive paste (Au, Ag) as equidistant dots.

## 2.2 Gas sensing measurements

To obtain an active functional layer, the sample-loaded IDE or pressed pellet is heated using a heater to a designated temperature. The activation temperature varies from 100 to 200 °C, depending on the type of material. This process is typically conducted in a closed environment under an inert gas atmosphere ($N_2$ or Ar) by applying a voltage bias (1–2 V for the IDE or up to 3–5 V for a pressed pellet). Under these conditions, the material attains a stable resistance value, and is considered as the baseline resistance, which is detected by a sourcemeter. Once stabilized, the material is exposed to the target analyte gas at different temperatures and varying concentrations to investigate the sensing behaviour of the sensing element, the MOF/COF in the present case. The gas switching and concentration adjustments are managed using mass flow controllers that precisely control the flow rates of the gases. Fig. 5 illustrates a schematic representation of the gas sensing setup, which includes a closed probe chamber with two probes, the sample material (in the form of a pellet or coated on the IDE), a heater, and inlet for gases to be introduced into the probe chamber. The heater is connected to a temperature control unit to maintain the required temperature, while the probes are interfaced with a sourcemeter and a computer for data acquisition. The performance of chemiresistive sensors is evaluated based on some key parameters, which collectively determine the accuracy and effectiveness of the sensor.[86–88] These parameters are described below.

**2.2.1 Sensitivity (S).** Sensitivity (S) in the context of chemiresistive sensors can be defined as the ratio of the change in
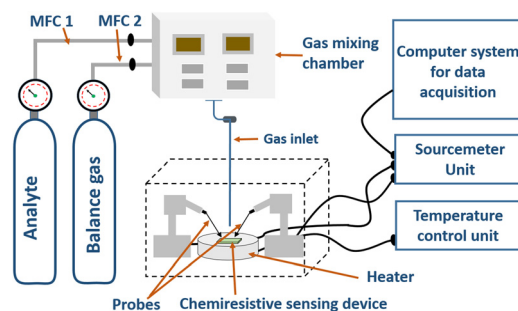


**Fig. 5** Schematic representation of the chemiresistive gas sensing setup commonly used in the literature.

resistance ($\Delta y$) of the active material to the unit change in gas concentration ($\Delta x$).[17,89]

$$S = \Delta y / \Delta x$$

where $\Delta y$ = change in the resistance of the material and $\Delta x$ is the change in concentration of the gas.

**2.2.2 Response ($R_S$).** The response ($R_S$) is calculated by measuring the difference in the electrical resistance of the sensor film after exposure to the target gas, compared to its resistance in the pristine state, that is, prior to exposure to the target gas. These modulations appear either as an increase or decrease in resistance, depending on the nature of the target gas and the type of sensor.[90] $R_S$ is calculated using different formulae as given below,

$$R_S = \frac{R_a - R_g}{R_a}$$

$$R_S \% = \frac{R_a - R_g}{R_a} \times 100$$

$$R_S = \frac{R_a}{R_g}$$

where $R_a$ is the resistance of the material stabilised under an inert gas, and $R_g$ is the resistance in the presence of the target gas. $R_a$ and $R_g$ are interchangeable depending on the reducing/oxidising nature of the target gas.

**2.2.3 Response time ($\tau_{res}$).** This refers to the time taken by the sensor to effectively interact with the target gas, inducing changes in its intrinsic resistance. It is the defined as time required by the sensor to achieve 90% of its maximum resistance when exposed to the target gas. Faster response times are generally preferred for real-time monitoring.

**2.2.4 Recovery time ($\tau_{rec}$).** This is the time required for the sensor to revert back to 90% of its initial resistance value after the supply of the target gas has been discontinued. Short recovery times are important for continuous monitoring.

**2.2.5 Limit of detection (LOD).** This is the lowest concentration of the target gas that the sensor can reliably detect under specific conditions. Often the sensitivity of the sensor is correlated to the LOD. The LOD can be determined using one of methods described below.

**2.2.6 Signal-to-noise ratio.** Generally, SNR = 3, is widely recognized as the standard for determining the LOD.[91]

**2.2.7 Linear regression.** LOD is calculated as three times the standard deviation of the response ($S_a$) divided by the slope of the calibration curve ($b$).[92]

$$\text{LOD} = 3S_a/b$$

**2.2.8 Root mean square (RMS) method.** Alternatively, LOD can be determined using the RMS approach, which involves statistical analysis to estimate the lowest concentration of analyte that can be reliably detected above background noise levels.

$$\text{LOD(ppm)} = \frac{3 \times \text{RMS (noise)}}{S}$$

$$\text{RMS (ppm}^{-1}) = \sqrt{V_x^2/N}$$

where RMS(noise) = root mean square (RMS) noise of the baseline, which is calculated using the variation method, $V_x^2 = \sum (Y_i - Y)^2$ values are the experimental data points of the baseline from the $\Delta R/R_a$ vs. time (s) plot, $Y_i$ and $Y$ are the measured data points and fitted curve values, respectively. $S$ is the slope of linear fitted data from $\Delta R/R_a$ of the sensor with the $H_2$ concentration (ppm), $N$ = number of data points.[93–95]

**2.2.9 Selectivity.** Selectivity indicates the ability of the sensor to specifically respond to a particular gas species among other interfering gases. It is a key attribute of the material that depends on factors such as its chemical affinity towards the target gas, the presence of specific binding sites, and the molecular morphology.
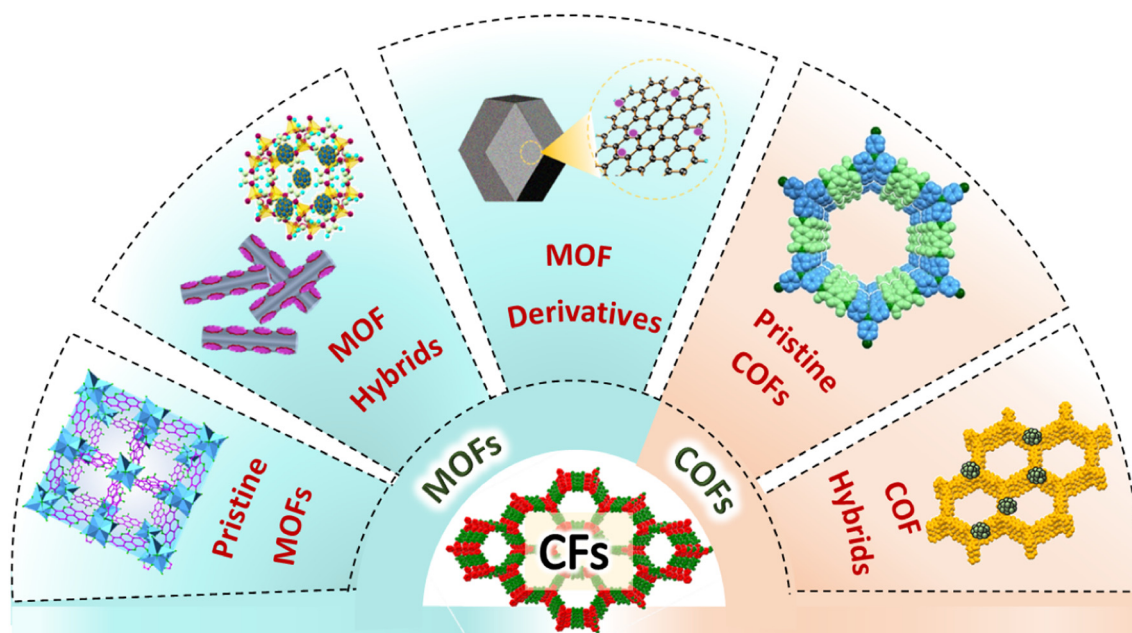
# 3. Porous CFs for chemiresistive $H_2$ sensing

The versatility of MOFs and COFs is being actively explored to develop effective $H_2$ sensors. Although MOFs and COFs both belong to the class of porous CFs and share similarities in their features, a clearer understanding of advancements in chemiresistive $H_2$ sensing requires a distinct classification. Thus, CFs have been divided into two sections, section 3.1 and 3.2, based on their structural diversity, the nature of studies reported, and the type of sensing mechanisms operating in these materials. Section 3.1 is dedicated to MOF-based $H_2$ sensors reported so far in the literature to the best of our knowledge. Section 3.2 highlights studies on COFs, demonstrating their potential as effective $H_2$ sensors. A schematic illustrating the classification of CF materials for $H_2$ sensing in the following discussion is given in Scheme 2.

## 3.1 Applications of MOFs for chemiresistive $H_2$ sensing

Leveraging the unique properties of MOFs to achieve optimum sensing performance for $H_2$ detection, some key approaches have been adopted in the literature; these include utilizing pristine/functionalized MOFs, applying a MOF passive layer to cover metal oxides for molecular sieving, integrating metal nanoparticles (MNPs) with MOFs to form hybrids, and employing materials that are derived from MOFs. Table 1 summarizes recent studies reported in the literature in this direction.

**3.1.1 Pristine MOFs.** A handful of reports on chemiresistive $H_2$ sensing using materials based on pristine MOFs have been published in recent times, with the first study reported in 2016,[96] suggesting the availability of ample opportunities to



**Scheme 2** Schematic illustration depicting the classification of CF materials into MOFs and COFs, along with their respective subdivisions for $H_2$ sensing applications.

**Table 1** Summary of the literature on MOF-based chemiresistive $H_2$ sensors

| S. no. | Material | Sensing temp. (°C) | $H_2$ conc. | Sensing properties | Response time (s) | Recovery time (s) | Limit of detection (LOD) | Selectivity | Ref. |
|---|---|---|---|---|---|---|---|---|---|
| Pristine MOFs | | | | | | | | | |
| 1 | ZIF-8/ZIF-67 | RT | 5 ppm | $\Delta R/R_0 = 81.6\%$ | 856 s | 905 s | 1 ppm | $C_7H_8$, CO, $NO_2$ and $C_2H_5OH$ | 100 |
| 2 | Zn-BDC-NH$_2$ | 50 | 10 ppm | $R_a/R_g = 2.93$ | ~40 s | ~50 s | 1 ppm | CO, $C_6H_6$, $C_7H_8$ and $CH_4$ | 101 |
| 3 | Co-MOF-I and Co-MOF-II | 200 | 50 ppm | $\Delta R/R_0 \times 100 = 53.8\%; 101.4\%$ | — | — | — | $NO_2$, CO, $O_2$, $H_2S$ | 102 |
| MOF@SMO hybrids | | | | | | | | | |
| 1 | ZnO@ZIF-8 NWs | 300 | 50 ppm | $R_{gas}/R_{air} = 1.44$ | — | — | 10 ppm | $C_7H_8$ and $C_6H_6$ | 96 |
| 2 | ZnO@ZIF-8 nanorods | 250 | 50 ppm | $\Delta I/I_0 = 80\%$ | — | — | 10 ppm | $C_6H_6$, $C_7H_8$, $C_2H_5OH$, and $CH_3COCH_3$ | 113 |
| 3 | ZnO@ZIF-8 | 275 | 50 ppm | — | 50 s | 130 s | — | $C_6H_6$ | 114 |
| 4 | 16-ZnO@ZIF-8 | 290 | 1000 ppm | $R_a/R_g = 6$ | — | — | — | $C_2H_6O$, $C_3H_6O$ | 115 |
| MNS@MOF hybrids | | | | | | | | | |
| 1 | Pd nanowire@ZIF-8 | RT | 1% | $\Delta R/R_0 = 3.5$ | 10 s | 7 s | 600 ppm | $O_2$ | 117 |
| 2 | Pt-Co-MOF@GO | 15 | 15 000 ppm | $\Delta R/R_0 = 9\%$ | 9 s | 12 s | 700 ppm | $CH_4$, CO, $CH_3OH$ and $CH_3COCH_3$ | 118 |
| 3 | ZnO@Pd@ZIF-8 nanowires | 200 | 50 ppm | $R_{gas}/R_{air} = 6.7$ | — | — | 10 ppm | $C_6H_6$, $C_7H_8$, $C_2H_5OH$, and $CH_3COCH_3$ | 119 |
| 4 | Pd/ZIF-67/PMMA | – | 1% | $\Delta I/I_0 = 24.1\%$ | 9.5 s (0.4% $H_2$) | 8.8 s (0.4% $H_2$) | 2 kPa | $C_6H_6$, $C_7H_8$, $C_2H_5OH$, CO and $CH_3COCH_3$ | 120 |
| 5 | Pd$^{II}$@CrPy | 60 | 1% | $\Delta R/R_0 = 2\%$ | 13 s | 10 s | 0.25% | $SO_2$, $NO_2$, CO, $CH_4$ and $CO_2$ | 126 |
| MOF-derived nanostructures | | | | | | | | | |
| 1 | ZnO@GC750 | RT | 5 ppm | $\Delta R/R_0 = 97.8\%$ | 34 s | 46 s | 0.1 ppm | HCHO, NO, $NH_3$, CO, $NO_2$ | 132 |
| 2 | ZIF-8rGO | 400 | 200 ppm | $\Delta R/R_0 = 18$ | 50 s | 7 s | 5 ppm | CO, $CH_4$, $NO_2$ and $C_2H_5OH$ | 133 |
| 3 | Co–ZnO–N/C | RT | 1% | $\Delta R/R_0 = 3.7\%$ | 26 s | 17 s | 0.25% | $SO_2$, $NO_2$, CO, $CH_4$ and $CO_2$ | 134 |
| 4 | MOF-derived $TiO_2$ | 30 | 1000 ppm | $R_a/R_g = 9.2$ | 17 s | 150–200 s | 25 ppm | CO, $C_3H_6$ | 135 |
| 5 | Sn-SIM-3 | RT | 5% | — | 400 s | 5–10 s | — | — | 136 |

explore pristine MOF-based $H_2$ chemiresistors. The synthesis of MOFs generally involves solvo/hydrothermal techniques at elevated temperatures and occasionally high pressures to obtain crystalline powders.[97] In recent times, methods for the preparation of thin films of MOFs under ambient conditions have also been developed.[98] ZIFs are a class of MOFs that are demonstrated to be versatile for many applications. They often display better thermal/chemical stabilities owing to the Co/Zn tetrahedrally coordinated to N-heterocyclic (for example: 2-methyl imidazole) based linkers. Among them, ZIF-8 with a zeolite sodalite (SOD)-type structure with a small aperture diameter of 3.4 Å and pore size of 11.6 Å was given more attention.[99]

Enhancing the sensing capabilities of one MOF over another by developing composites of two MOFs (MOF@MOF) was reported by D. Matatagui et al. They combined ZIF-8 and ZIF-67 [Co(mIm)$_2$, mIm = 2-methyl imidazole] into one composite with a molar ratio of 1 : 1. The ZIF-8/ZIF-67 composite was active for the sensing of $H_2$ gas at 180 °C.[100] The selectivity between $H_2$, $C_7H_8$, $C_2H_5OH$, CO, and $NO_2$ were compared. However, the responses towards $H_2$ and $C_7H_8$ using the ZIF-8 + ZIF-67 composite were comparable and there was scope for improvement. In addition, insights into the $H_2$ interactions with the MOF surface were not provided by this study. In principle, ZIF-8 and ZIF-67 are almost insulators and do not possess active sites for $H_2$. They may show n-type behaviour similar to that observed for ZnO. The effect of $H_2$ detection may be attributed to the presence of trace amounts of ZnO impurities that are formed during the synthesis of ZIF-8.

The functionalization of MOFs is a very straightforward approach, as shown in Scheme 3 and this was explored by H. W. Kim et al. for sensing $H_2$ at 50 °C by developing an amine-functionalized Zn-based MOF (Zn-BDC-NH$_2$).[101] A maximum response of $R_{air}/R_{gas} = 2.93$ and response/recovery times of 44/160 s, respectively, towards 10 ppm $H_2$ were observed. The $H_2$ sensing characteristics were attributed to the redox reactions occurring on the surface of the MOF between $H_2$ and adsorbed oxygen. D. K. Nguyen et al. demonstrated two Co-MOF-74 materials (Co-MOF-I = $C_{99}H_{54}N_9O_{45}Co_9$ and Co-MOF-II = $C_{72}H_{36}N_9O_{45}Co_9$) for $H_2$ sensing applications.[102] The pore apertures of Co-MOF-I and Co-MOF-II are 27.6 Å and 23.2 Å and they possess a high density of +2 and +3 states of Co ions. The MOFs were synthesized via a solvothermal route at 100 °C and activated using anhydrous methanol in supercritical $CO_2$ to achieve guest-free MOF structures. The MOF
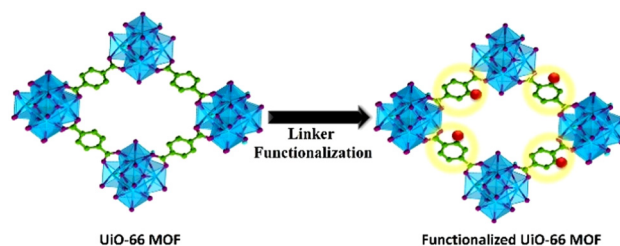


**Scheme 3** Schematic representation showing linker functionalization in MOFs.

samples were dispersed in 2-propanol and dropcast on Pt-interdigitated electrodes for further sensing experiments. The $H_2$ sensing studies were carried out at 200 °C in the presence of 50 ppm $H_2$. Co-MOF-I and Co-MOF-II showed responses ($S\%$) of 53.8 and 101.4%, respectively. The selectivity was tested and the sequence of the response was as follows: $H_2$ > $NO_2$ > CO > $O_2$ > $H_2S$, which depended on the molecular diameter of the gas, with the exception of CO gas. Furthermore, the high density of unsaturated Co ions also aided in increasing the response/sensitivity towards $H_2$. This was also compared with MOF-74, containing different metal clusters (Ni and Mg), which displayed a much lower response to $H_2$ (1.3 to 3.9%) at 200 °C. However, the actual role played by the Co ions in the MOFs that leads to the higher response to $H_2$ is unclear.

Although the examples on pristine MOFs discussed in section 3.1.1 have shown potential for the chemiresistive sensing of $H_2$, they are plagued by inherent challenges of limited charge migration and poor electrical conductivity. Moreover, this results in inferior signal transduction at low temperatures and it is essential to heat the samples for the hopping transport of electrons to prevail throughout the surface of the MOF. Also, these studies have not highlighted the role of $H_2$ selectivity. In order to address inherent challenges of pristine MOFs, the hybridisation of MOFs with semiconductor metal oxides and metal nanoparticles (Pd/Pt) has been developed. Section 3.1.2 discusses the studies reported on MOF hybrids for $H_2$ sensing and highlights their advantages over pristine MOFs.

**3.1.2 MOF hybrids.** MOFs have been hybridised with SMOs (MOF@SMO) or metal nanostructures (MNS@MOF) to enhance their synergistic sensitivity towards $H_2$. This section on MOF hybrids is further divided into two sub-sections: section 3.1.2.1 discusses studies reported on hybrids of SMOs and MOFs. These reports are limited to the role of the MOF as a molecular sieving layer to improve the selectivity of SMOs towards $H_2$. Apart from the gas sieving capabilities, as observed in the case of MOF@SMO hybrids, the hybrids of MNS@MOF also demonstrate the importance of an efficient charge transfer phenomenon for achieving superior $H_2$ sensing performance. Section 3.1.2.2 describes studies reported on MOFs decorated with metal nanostructures (MNS@MOF).

*3.1.2.1 Hybrids of MOFs with semiconductor metal oxides (MOF@SMO).* Most of the MOF hybrids have been demonstrated to act as molecular sieves owing to their well-defined porous structures with the exception of some studies discussed in section 3.1.2.2. The molecular (gas) sieving ability of MOFs provides unique advantages to realize better sensitivity in comparison with non-MOF based materials in gas sensing applications. Two effects, namely, the pre-concentration effect and the shape/size exclusion effect, can govern the sensitivity and selectivity of MOF-based sensors, respectively.[103] Molecular sieving is traditionally a non-equilibrium kinetic separation that depends mainly on the following factors: (a) gas diffusivity, (b) temperature, (c) pressure and (d) framework structure (pore size). Molecular sieving typically does not involve any

strong binding sites unlike those in the case of equilibrium separations.[104] However, due to extremely low diffusion kinetics of certain gases, energy provided in the form of heat (temperature dictated by the environment) and pressure (dictated by the gradient concentration) plays a crucial role in determining the selectivity of the MOF for a given gas.[103]

One of the well explored MOF-based micromembranes is ZIF-8 ($Zn(MeIM)_2$, MeIM = 2-methylimidazole) with a pore aperture of 3.4 Å (as determined by single crystal XRD). The pore aperture is flexible as a result of rotation of the MeIM linker and can be tunable in the range of 4 to 4.2 Å.[105,106] ZIF-8 has offered a kinetic separation-based selectivity not only for gas molecules with a molecular diameter comparable to the pore-aperture size but also for larger molecules like *para*-xylene at high temperatures.[107] Studies demonstrating the permeability of ZIFs for $H_2$ gas, and thus permitting effective selectivity over other gas molecules, are well reported.[108,109] The surface of traditional SMOs, like ZnO, $SnO_2$, *etc.* have been modified by growing a suitable ZIF micromembrane (Scheme 4). Nanorods/nanowires of these SMOs have advantages over spherical nanoparticles in terms of their larger surface area for the adsorption of gases and to achieve good sensitivity, in addition to possessing facile percolation paths for conduction.[110] It should be noted that the $H_2$ sensitivity using bulk/pristine SMOs like ZnO is not adequate. In general, ZnO is a direct band gap semiconductor material possessing numerous oxygen vacancy sites with no specific interactions for $H_2$. ZnO is an active sensor only when these oxygen vacancies are made available at high operating temperatures.[111] For example, a study on ZnO nanorod arrays showed a response ($\Delta R/R$) of 0.1% in the presence of 0.1% $H_2$ at 350 °C.[103] In another study, ZnO nanoassemblies showed a response of 11% for 0.5% $H_2$ at 400 °C.[112] Selectivity to a target gas is one of the major concerns with ZnO-based sensors that often results in mixed signals. The main objective of improving the selectivity of ZnO for $H_2$ has led to researchers modifying the ZnO surface by coating it with an appropriate material like MOFs. The design of MOF-based membranes to enhance the selectivity of ZnO towards $H_2$ was first explored by M. Drobek *et al.* using 10 wt% of ZIF-8 as a molecular
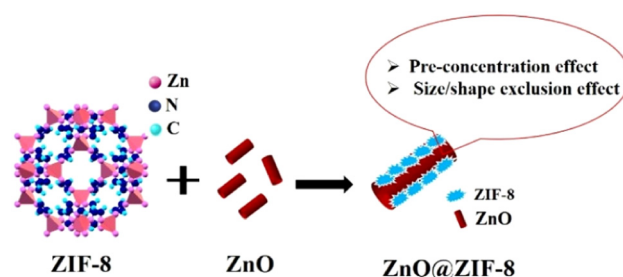
**Scheme 4** Schematic representation of the coating of ZnO nanorods using ZIF-8 to yield the ZnO@ZIF-8 composite. Pre-concentration and size/shape exclusion effects are two mechanisms that govern the $H_2$ interaction/permeability in the ZnO@ZIF-8 composite based $H_2$ chemiresistor.

sieving element that was grown on n-type ZnO nanowire (with a length of 25 μm) with ZnO thin films and 2-methyl imidazolate linker solution (Fig. 6).[96] The nanowires (NWs) of the ZnO core were encapsulated with a ZIF-8 shell/layer of 50–250 nm and exhibited a surface area of $1760 \pm 260$ m$^2$ g$^{-1}$. The devices fabricated using ZnO@ZIF-8 NWs demonstrated the selective sensing of H$_2$ at 300 °C and showed a maximum response of $R_{air}/R_{gas} = 1.44$ (where $R_{air}/R_{gas}$ are the resistance of the chemiresistor in the presence and absence of H$_2$) towards 50 ppm of H$_2$. In this case, it is reported that ZIF-8 acts as a selective membrane barrier and permits more diffusion of small H$_2$ molecules (kinetic diameter = 2.89 Å) compared to larger C$_7$H$_8$ and C$_6$H$_6$ molecules (kinetic diameter = 5.92 Å and 5.27 Å, respectively). Analogous to this study, T. Zhou et al. demonstrated the applicability of two different MOF coatings, namely, ZIF-8 and ZIF-71 [Zn(dcIm)$_2$, dcIm = 4,5 dichloroimidazole] grown on a ZnO nanorod array (NRA) for selective H$_2$ sensing.[113] ZnO@ZIF NRAs were synthesized by utilizing self-assembling templates of ZnO NRAs to provide the Zn$^{2+}$ metal ions, followed by solvothermal treatment. In the case of ZnO@ZIF-8 NRAs, the ZIF-8 shell thickness was reported to be 70–100 nm whereas, for ZnO@ZIF-71 NRAs, the ZIF-71 shell thickness was optimised to be 50 nm. The H$_2$ sensing characteristics were compared between ZnO NRAs, ZnO@ZIF-8 NRAs and ZnO@ZIF-71 NRAs at 250 °C. ZnO@ZIF-8 NRAs were able to selectively detect H$_2$ over benzene (5.85 Å), ethanol (4.53 Å), and acetone (4.60 Å), owing to the presence of the smaller pore aperture of ZIF-8 (3.4 Å). Conversely, ZnO@ZIF-71 NRAs show a selective response towards ethanol and acetone as the pore aperture of ZIF-71 is between 4.8 and 5.4 Å, and hence, enable gas permeation with ease.
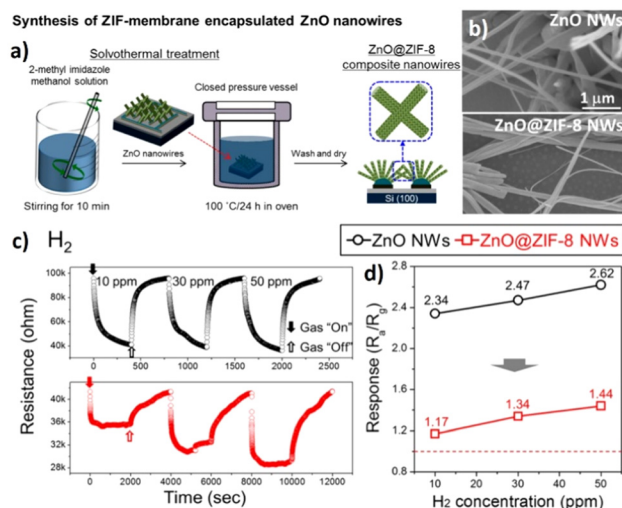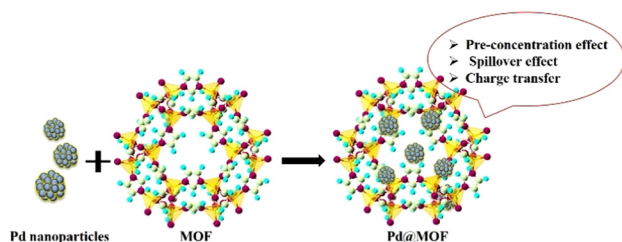


**Fig. 6** (a) Schematic of the synthesis steps yielding the ZIF-membrane encapsulated ZnO nanowires (ZnO@ZIF-8 NWs), (b) FESEM images of networked ZnO nanowires and ZnO@ZIF-8 composite nanowires, (c) and (d) responses of the pristine ZnO nanowires and ZnO@ZIF-8 composite nanowires in contact with 10, 30, and 50 ppm H$_2$ gas. Reproduced with permission from ref. 96, American Chemical Society, copyright@2016.

Another report by A. I. Khudiar et al. reported the encapsulation of ZnO nanorods (NRs) using ZIF-8 to form a hybrid and was termed ZnO@ZIF-8.[114] Thin films of ZIF-8 were synthesized on Al$_2$O$_3$ substrate via a solvothermal and sacrificial template route similar to the self-assembling template route used by T. Zhou et al. described above.[113] Platelet-like structures of ZIF-8 were coated on ZnO NRs (~7 μm length); this was evident from electron microscopy studies. The optimal sensing temperature was reported to be 275 °C and the selectivity studies compared H$_2$ and benzene. The transport limitation offered by the ZIF-8 coating over ZnO NRs enabled H$_2$ to be selectively detected with response and recovery times of 50 s and 130 s. Although, the pristine ZnO NRs lacked the selective detection of H$_2$, the response and recovery times were shorter than those of the ZnO@ZIF-8-based sensor. This was ascribed to the uninterrupted interaction between H$_2$ and the uncoated ZnO surface. Notably, the thickness of the MOF coating on ZnO nanostructures plays a significant role in sieving and sensing H$_2$. Studies carried out by S. Zhang et al. demonstrated the effect of the ZIF-8 film thickness coated on ZnO nanostructures; this was achieved via altering the processing time of ZIF-8 film formation.[115] Sensor studies demonstrated that 1000 ppm H$_2$ was optimum when the measurement was carried out at 290 °C. The molecular sieving effect of the ZIF-8 film on ZnO particles was more effective at sensing H$_2$ only with a growth time of >8 h with >100 nm thickness. Among the synthesized hybrids, 16-ZnO@ZIF-8 showed a response of $R_{air}/R_{gas} = 6$ towards 1000 ppm H$_2$. The selectivity studies were carried out for C$_2$H$_6$O and C$_3$H$_6$O. The pore aperture size of ZIF-8@ZnO is ~4 Å, which is larger than H$_2$ = 2.89 Å, and smaller than C$_2$H$_6$O = 4.53 Å and C$_3$H$_6$O = 4.60 Å. A smaller gas molecule like H$_2$ could interact with the ZnO core more easily than C$_2$H$_6$O and C$_3$H$_6$O.

The above discussed literature explores using ZIF-based MOF encapsulated ZnO nanostructures (ZnO@MOF composites) to improve H$_2$ sensor selectivity. However, thicker ZIF films over ZnO can occlude the adsorption of even H$_2$ gas, thus decreasing the sensitivity of the sensor. Optimization of the uniform ZIF shell coating is a crucial step to improve the sensitivity of ZnO@MOF composites for H$_2$ sensing. Furthermore, the studies discussed so far have only demonstrated the selectivity of ZnO@MOF in the presence of molecules that are much bigger (in terms of kinetic diameter) than H$_2$, for example, C$_7$H$_8$, C$_6$H$_6$, C$_2$H$_6$O and C$_3$H$_6$O. Despite this fact, investigation of the selectivity of ZnO@MOF composites towards small gas molecules, like CO, CO$_2$, SO$_2$ and NO$_x$, which have kinetic diameters close to that of H$_2$, is essential. Moreover, redox-active SMOs like SnO$_2$, CeO$_2$, Fe$_2$O$_3$, Co$_3$O$_4$ etc. as the core coated with a suitable MOF layer have not been explored for H$_2$ sensing.

*3.1.2.2 Hybrids of MOFs decorated with metal ions/nanostructures (MNS@MOF).* Functionalization of MOFs with metal ions/nanostructures is another approach to achieve enhanced performance. The incredible features of MOFs, especially ZIF-8, which exhibit good permeability for H$_2$ and ease of synthesis, as detailed in section 3.1.1, have led researchers to explore functionalizing MOFs with nanostructures. Among all

the noble metals, Pd is a good chemisorption component that can interact with $H_2$ under ambient conditions *via* interstitial metal hydride ($PdH_x$) formation, as discussed in Section 1.[116] Pd nanoparticles (NPs) are either confined to the pores of MOFs or they are highly dispersed on the MOF matrix (Scheme 5). Although these Pd-based $H_2$ sensors display very fast response times, they are limited to detecting $H_2$ only at lower concentrations (1–2% max). On the other hand, the sensitivity of Pd-based sensors is known to degrade in the presence of gases like $O_2$, CO, $SO_2$ and $H_2S$ due to the formation of strong Pd–O intermediates, giving water as a by-product.[116] As a result, the kinetics/rate of $H_2$ adsorption will not only decrease but also block the adsorption sites on the Pd surface for further adsorption of gases. W.T. Koo *et al.* optimised the self-assembled growth of ZIF-8 on Pd NWs to address the interference in sensing $H_2$ caused by the presence of $O_2$ gas.[117] The primary step in preparing Pd NWs@ZIF-8 is to synthesize Pd NWs (diameter = 200 ± 50 nm) followed by growing a layer of ZIF-8 using a nanofiltration method. Pd NWs@ZIF-8 were self-assembled over 2–6 h to obtain a maximum thickness of 330 nm of ZIF-8 layer grown on the surface of Pd NWs. The gas sensing characteristics were tested as a function of the thickness of the ZIF-8 coating on Pd NWs obtained at different time intervals (2 h to 6 h). Pd NWs@ZIF-8_4 h exhibited the highest response of 3.5% towards 1% $H_2$ at room temperature. The response and recovery times were 10-fold faster than those of pristine Pd NWs. The sensing mechanism was explained by the molecular sieving effect of ZIF-8, which further enhanced the kinetics of response and recovery in the presence of $H_2$. In another study, nanocomposites of Pt NPs, Co-BDC MOF (BDC = 1,4 benzene dicarboxylic acid) and graphene oxide (GO) based p-type sensors were demonstrated by S. Fardindoost *et al.*[118] Pt was sputtered on Co-MOF@GO that was synthesized by a solvothermal route using as-synthesized GO powder and $Co(NO_3)_2 \cdot 6H_2O$ and a BDC linker. A flower-like morphology with an interlayer distance of 0.43 nm in GO–Co was observed. The optimum sensing temperature was reported to be 85 °C. Pt-sputtered Co-MOF@GO showed a response of $\Delta R/R_0$ = 10% towards 1.5% $H_2$. The response and recovery times are reported in the range of 216–230 s. The interaction between $H_2$ and Pt-sputtered Co-MOF@GO is known to facilitate the formation of $Pt–H_x$ intermediates, which undergo

redox reactions that occur on the surface of GO. In another study, M. J. Weber *et al.* prepared Pd NPs (prepared by an atomic layer deposition method) decorated on ZnO with ZIF-8 membrane (ZIF-8/Pd/ZnO) to enhance the selectivity of ZnO NWs for $H_2$ sensing and achieved a maximum signal response.[119] The optimal sensing temperature was reported to be 200 °C and the highest response of $R_{air}/R_{gas}$ = 6.7 for 50 ppm $H_2$ was observed (Fig. 7). Although the response of Pd/ ZnO NWs was ~20% greater than that of ZIF-8/Pd/ZnO, it failed to outdo ZIF-8/Pd/ZnO in terms of selectivity towards $C_6H_6/C_2H_5OH/C_7H_8/CH_3COCH_3$. Three factors are reported to influence the sensor performance; (a) concentration effect of the ZIF-8 membrane, (b) spill-over effect of Pd NWs and (c) redox reactions on the surface of ZnO NWs. It should be noted that often $H_2$ gas produced from the steam reforming of methane is contaminated with CO. It is essential to decipher the $H_2$ sensor characteristics in the presence of CO for real-time applications. In order to address the detrimental effect of the presence of CO on the sensing characteristics of Pd-based nanostructures for $H_2$ sensing, the Pd/ZIF-67/PMMA [PMMA = poly(methyl methacrylate)] based sensing element was reported by B. Xie *et al.*[120] The composite material consisted of a MOF as an intermediate layer between the Pd nanocluster and PMMA polymer. The synergistic effects of ZIF-67 and PMMA membrane impacted the electronic structure of Pd NCs
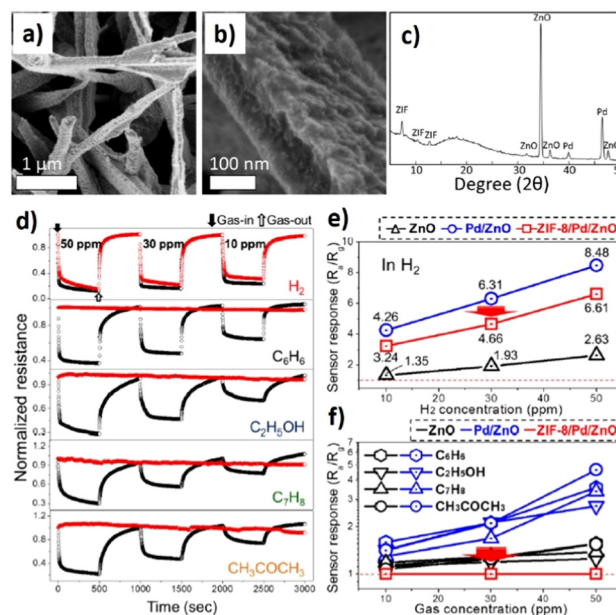
**Fig. 7** (a and b) SEM images of ZIF-8/Pd/ZnO NWs, (c) GI-XRD diffraction pattern (the ZIF-8, ZnO and Pd peaks are indicated), (d) dynamic normalized resistance curves of Pd/ZnO and ZIF-8/Pd/ZnO NW gas sensors when the devices were exposed to 10, 30 and 50 ppm $H_2$, $C_6H_6$, $C_2H_5OH$, $C_7H_8$ and $CH_3COCH_3$ gases, (e) calibration curves obtained using bare ZnO, Pd/ZnO and ZIF-8/Pd/ZnO NW-based gas sensors, (f) calibration curves of bare ZnO, Pd/ZnO and ZIF-8/Pd/ZnO NW gas sensors to 10, 30 and 50 ppm $H_2$, $C_6H_6$, $C_2H_5OH$, $C_7H_8$ and $CH_3COCH_3$ interfering gases. Reproduced with permission from ref. 119, American Chemical Society, copyright@2018.

**Scheme 5** Schematic representation of the decoration of a MOF (example: ZIF-8) with Pd nanoparticles/clusters to give Pd@MOF composites. Pre-concentration, spillover and the charge transfer effect are three mechanisms that govern the $H_2$ interaction/permeability.

(NCs = nanocubes). Pd/ZIF-67/PMMA showed the highest response of $\Delta I/I_0 = 24.1\%$ towards 1% $H_2$. The response and recovery times were in the range of 8–10 s in the presence of 0.4% $H_2$. The authors proposed that PMMA acted as a permeable layer for $H_2$ whereas ZIF-67 assisted in enhancing the sensitivity and improving the response/recovery times. It was also reported that the Pd/ZIF-67/PMMA sensor showed a high tolerance towards CO poisoning because of the PMMA layer, as compared to that observed in the case of pristine Pd and Pd/ZIF-67. Selectivity studies with volatile organic compounds – VOCs ($C_6H_6$, $CH_3COCH_3$, $C_7H_8$, $C_2H_5OH$) – using Pd/ZIF-67/PMMA revealed that the sensor did not show any response to VOCs, thus exhibiting high selectivity.

The rapid development of electrically conductive 2D MOFs is another driving force that has led to increased research in developing MOFs as sensing elements in chemiresistive sensing.[67,121] The research groups of Mircea Dincă and Martí-Gastaldo have extensively investigated electrically conductive MOFs for the detection of VOCs and small molecules.[53,122] Additionally, the phase of developing redox-active MOFs has been highly sought after in recent times.[123] In fact, the MOFs synthesized traditionally using metal centres like Zn(II) and carboxylates (e.g. BDC) or imidazolates (2-MeIM) are often redox inactive.[124] The construction of MOFs using 3d transition metal centres (first row transition series) that show redox-state changes may often result in changes to the topology/geometry of the product MOF. Besides, the use of redox-active ligands can lead to the availability of radical states (e.g. anion radicals of pyrazine ligands) but require an inert atmosphere during synthesis.[123] In an attempt to design 2D conductive MOFs using transition metal ions with strongly reducing features in conjugation with organic linkers, K. S. Pedersen et al. synthesized $CrCl_2(pyz)_2$ [$Cr^{III}Cl_2(pyz)_2$, pyz = pyrazine] for the first time. $CrCl_2(pyz)_2$ showed a strong degree of $\pi$–d conjugation and strong redox activity was displayed by the pyrazine ligand.[125] Instead of an ionic conduction pathway through the pores, the movement of electrons/holes (charge transfer phenomenon) through the framework was reported to influence the redox activity. Inspired by fascinating structure dependent properties displayed by the redox-active $CrCl_2(pyz)_2$ MOF, our group investigated the use of $CrCl_2(pyz)_2$ as a sensor element in a chemiresistor configuration for $H_2$ sensing (Fig. 8).[126] The sites responsible for the interactions with $H_2$ in the target gas were systematically studied by anchoring Pd(II) ions on $CrCl_2(pyz)_2$. It was observed that the $CrCl_2(pyz)_2$ MOF enabled a high dispersion of Pd(II) through charge transfer interactions, occurring in the vicinity of the negatively charged pyrazine linker. $Pd^{II}$@CrPy showed a response of $\Delta R/R_0 = 2\%$ towards 1% $H_2$ concentration at 60 °C. The response and recovery times were in the range of 5–8 s. The limit of detection for $H_2$ was found to be 0.25%. $Pd^{II}$@CrPy displayed reversible and long-term stability towards $H_2$ via a partial charge transfer mechanism demonstrated through density functional theory (DFT) calculations. In this study, an inert atmosphere of $N_2$ was used as a background gas unlike in the previous studies described wherein
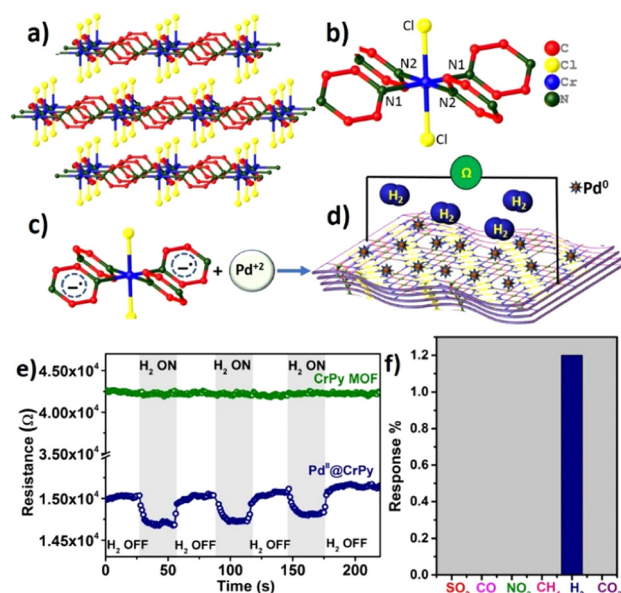


**Fig. 8** Structures of $CrCl_2(pyrazine)_2$ MOF and $Pd^{II}$@$CrCl_2(pyrazine)_2$: (a) staggered stacking layers of $CrCl_2(pyrazine)_2$, (b) secondary building unit in $CrCl_2(pyrazine)_2$, (c) pyrazine anion radical in ligand reaction with $Pd^{2+}$ precursor, (d) chemiresistive sensing of $H_2$ using $Pd^{II}$@$CrCl_2(pyrazine)_2$, (e) comparison of the gas sensing performance of CrPy and $Pd^{II}$@CrPy to 1% $H_2$ gas; response−recovery curves of $Pd^{II}$@CrPy for 1% $H_2$ and (f) selectivity studies of gases tested near their TLV limits include 10 ppm $SO_2$, 10 ppm CO, 10 ppm $NO_2$, 0.05% $CH_4$, 0.5% $H_2$ and 0.5% $CO_2$. The figure is reproduced with permission from ref. 126, Elsevier, copyright@2022.

air was majorly used. This particular study gives an insight into sensing $H_2$ above ppm levels using 2D conductive MOFs.

It should be noted that the majority of studies described in this section have demonstrated $H_2$ sensing at ultra-low ppm levels. The detection of $H_2$ in the range of 1–4% is also a great challenge as the sensing surface begins to get saturated at these concentrations. Composites of Pd/Pt@MOFs are very attractive for room temperature sensing; however, the stability and sluggish recovery speeds pose challenges for their $H_2$ sensing proficiencies. Downsizing Pd/Pt NPs to atomic levels and high dispersion could overcome some of the glitches associated with metal surface saturation attributed to the formation of $\beta$-$PdH_x$ systems in the future.

**3.1.3 MOF-derived nanostructures (metal oxides derived from MOF templates).** In this section, studies on pyrolyzing MOFs and using a MOF-templated route to derive metal oxide nanostructures and graphitic carbon-based materials are discussed. MOFs have been used as self-sacrificing precursors/templates for creating carbon-rich materials, various metal oxide nanostructures, carbides, nitrides, sulfides and phosphides (Scheme 6).[127] These MOF-derived nanomaterials can offer many advantages compared to the nanostructures originating from non-MOF-derived precursors and these include, (a) large surface area, (b) abundant active sites, (c) high degree of porosity, (d) reasonably straightforward structural transformation and (e) control over the degree of graphitization and
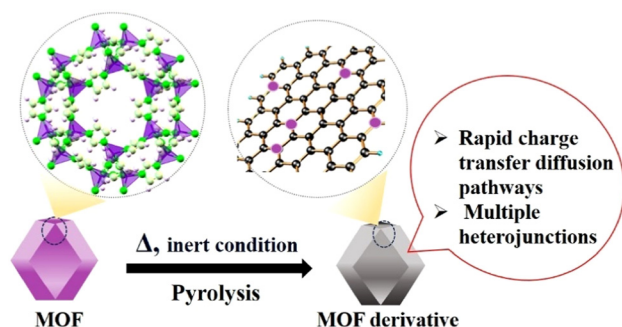
**Scheme 6** Schematic showing the pyrolysis of the pristine MOF to its derivative, wherein the MOF derivative contains an extensive network of doped carbon and metal oxide nanostructures. Rapid charge diffusion and multiple heterojunctions are two major mechanisms for sensing $H_2$ in MOF-derived materials.

crystallinity of the end-product. All these characteristic features can be tuned by a suitable choice of the parent MOF and the right amalgamation of conditions such as pyrolysis temperature, composition of the reaction gas/gas mixture, heating rate and pyrolysis time.[128] Nonetheless, the unavoidable partial/complete destruction of MOFs, which results in a reduction of the overall surface area and porosity to obtain MOF-derived nanomaterials with superior performances compared to their conventional bulk counterparts, will always be a concern. However, MOF-derived nanomaterials stand out in various areas of applications compared to pristine MOFs due to the benefits of having a more condensed carbon network (graphitic carbon), good charge transport, high electrical conductivity, and high thermal and chemical stability.[129] Over time, the limitation associated with the conductivity of pristine MOFs has been overcome by developing MOF-derived nanostructures; this has further broadened their scope for sensing applicability. The majority of studies have been directed towards sensing VOCs and $NO_x$; however, $H_2$ sensing studies have been slowly attracting attention from the research community.[130,131] Sharma et al. synthesized an ethylenediaminetetraacetic acid (EDTA) chelated ZIF-8 framework by high temperature calcination (550, 650, and 750 °C) under an Ar atmosphere to obtain ZnO@GC (GC = graphitic carbon).[132] Electron microscopy studies confirmed the formation of truncated hexagonal-like polyhedra (~230 nm). A chemiresistor fabricated using ZnO@GC-750 demonstrated a superior $H_2$ sensing performance at room temperature with 97.8% response towards 5 ppm of $H_2$. The response/recovery times were in the range of 34–46 s with a LOD of 0.1 ppm. The sensing characteristics were also superior when compared to those of pristine ZnO-750 (prepared using a conventional approach, non-MOF derived). In this study, the sensing features can be corroborated by the enhancement in $H_2$ interactions in addition to the presence of multiple p–n heterojunctions at the interface of n-type ZnO and p-type GC in ZnO@GC-750. S. Zhou et al. used an approach of functionalizing ZIF-8-derived ZnO with reduced graphene oxide (rGO).[133]

Sheets of rGO contained homogeneously dispersed ZnO NPs, which maintained the rhombic dodecahedron morphology (~250 nm) of the ZIF-8 precursor. The ZnO/rGO composite was active for sensing $H_2$ at 400 °C. The rGO contributed to the increased conductivity of the ZnO/rGO composite and enhanced the selectivity of pristine ZnO, with a response of $I_g/I_0 = 18$ ($I_g$ and $I_0$ are the sensor DC currents in a target gas and ambient air, respectively) and response/recovery times of 50/7 s towards 200 ppm of $H_2$. However, the sensing temperatures in this study are quite high and are in the same range as those required for pristine SMOs. Our group reported a room temperature $H_2$ sensor using bimetallic Co/Zn-ZIF-derived Co-doped ZnO nanostructures.[134] Co–ZnO–N/C (N/C refers to nitrogen-doped carbon) possessed a high dispersion of $Co^{2+}$ (2.3 wt%) active sites on amorphous ZnO–N/C and showed a response of 3.4% and fast response/recovery times in the 17–26 s range. The sensing characteristics of Co–ZnO–N/C were superior to those of ZnO–N/C (Fig. 9). The presence of $Co^{2+}$ was found to be responsible for sensitizing the Co–ZnO–N/C nanostructure followed by a rapid charge transfer diffusion pathway provided by nitrogen-doped carbon. M. Guo et al. fabricated a miniature $WO_3$–C/$In_2O_3$ micro-electro-mechanical system (MEM)-based sensor for $H_2$ detection.[135] $In_2O_3$ is derived from MIL-68 (In) MOF (molecular formula: $C_{25.5}H_{12}In_3N_{0.5}O_{15.5}$) followed by an optimum loading of $WO_3$ (9 wt%) and subjecting the material to further calcination. $WO_3$–C/$In_2O_3$ responded to $H_2$ with a maximum response of $R_a/R_g = 10.11$ and response/recovery times of 1.9/9 s. The enhanced sensing characteristics are attributed to the presence of multiple heterojunctions (n–n and p–n) between $In_2O_3$, $WO_3$ and carbon material, which are responsible for increasing the number of chemisorbed oxygen species and oxygen vacancies. $TiO_2$ nanotablets derived from MIL-125 were reported for $H_2$ sensing at room temperature by utilizing the advantages of the presence of abundant oxygen vacancies and porous nature of the material.[136] MIL-125 was calcined at 400 °C and the resulting sample (MOF-derived $TiO_2$) displayed a regular morphology of square nanotablets in the range of 200 to 300 nm, as confirmed by electron microscopy studies. A response of 9.2 for MOF-derived $TiO_2$ was reported, which was ~5 times higher than that of pristine $TiO_2$ (synthesized via non-MOF pathway). Moreover, a response time of 17 s exhibited by MOF-derived $TiO_2$ was higher than that of pristine $TiO_2$ (6000 s). The gas sensing mechanism was attributed to the redox reactions occurring on the surface of $TiO_2$.

The examples discussed above are some of the rare studies in the direction of using non-noble metals for chemiresistive sensing of $H_2$. A MOF-derived route for developing room temperature $H_2$ sensors may be quite attractive research in terms of academic curiosity. However, arguably MOFs may offer certain practical limitations like longer synthetic methodologies and the use of very high calcination temperatures (600–800 °C).

### 3.2. Application of COFs for chemiresistive $H_2$ sensing

The significant structure–property relationship has rendered COFs intriguing materials for multiple functionalities includ-
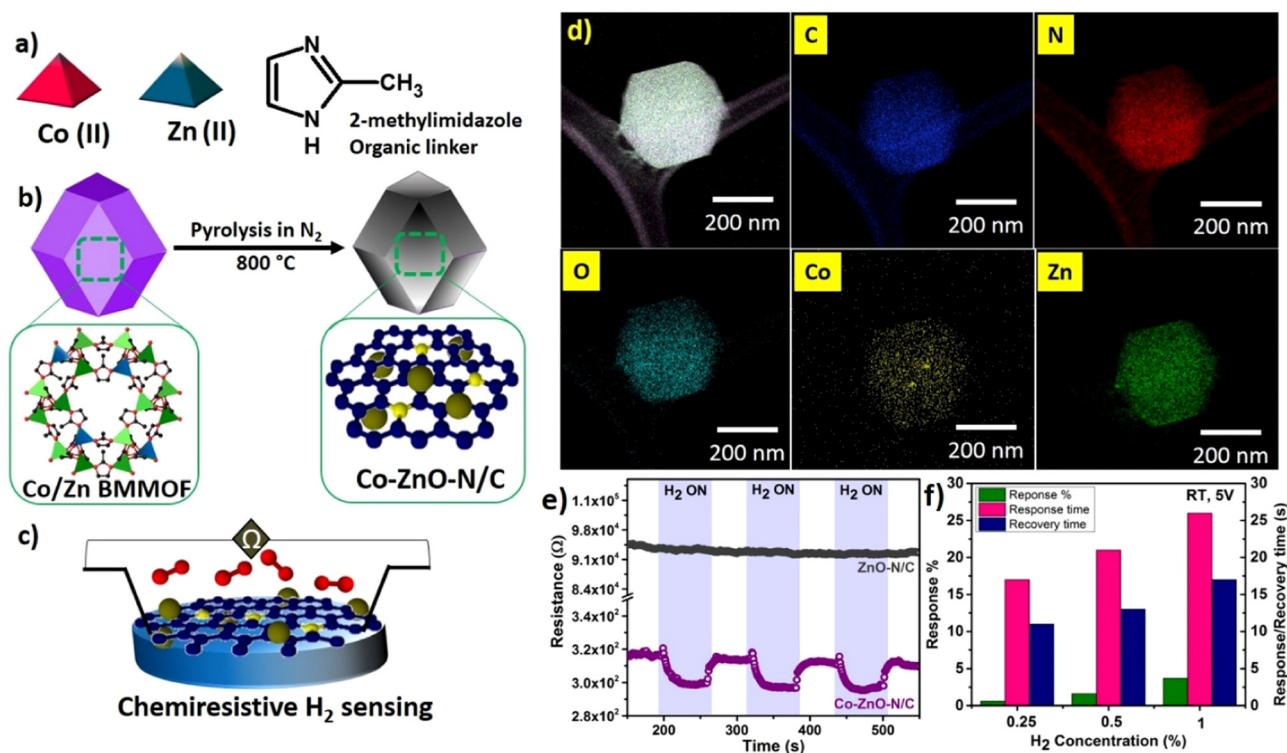
**Fig. 9** (a) Precursors used for the synthesis of Co/Zn bimetallic MOF (BMMOF), (b) pyrolysis of Co/Zn BMMOF to form Co−ZnO−N/C, and (c) chemiresistive sensing of $H_2$ using Co−ZnO−N/C, (d) high annular dark-field imaging by using a scanning transmission electron microscope with energy-dispersive X-ray spectroscopy (EDS) mapping of C, N, O, Co, and Zn; (e) comparison of the gas sensing performance of Co−ZnO−N/C and ZnO−N/C for 1% $H_2$ gas and (f) effect of $H_2$ concentration (0.25, 0.5, and 1%) on the overall gas sensing characteristics at room temperature. Reproduced with permission from ref. 132, American Chemical Society, copyright@2023.

ing gas adsorption, energy storage devices, optoelectronic devices, catalysis, chemical sensing, and bio-related applications.[137–142] Initially, COFs were perceived as less optimal materials for chemiresistive gas sensing applications compared to other uses, primarily due to their inherent bulky nature and low conductivity. Through efforts over the past decade, COFs have gradually emerged in chemiresistive sensing applications, effectively detecting gases such as $NO_2$, $CO_2$, $NH_3$, VOCs and humidity.[143–145] However, the potential of COFs for sensing $H_2$ gas has been overlooked. In this section we discuss the emerging prospects of COFs as chemiresistive $H_2$ gas sensors. A summary of the literature on COF-based chemiresistive $H_2$ sensors is provided in Table 2.

In the context of $H_2$ sensing, there has been limited exploration of using COFs. The bulkiness of COFs results from the dense stacking of layers driven by π–π interactions, leading

to hindered access to the active sites.[146] It is rather a challenge to fabricate sensors using bulk materials, as it often results in inhomogeneous films due to poor dispersibility in solvents. The unstable suspensions pose difficulties in device fabrication and impact sensor performance.[147,148] Addressing these issues, COFs have been delaminated into nanosheets that exhibit improved functionalities including high efficiency for energy storage, enhanced gas adsorption, ion diffusion and better processability, compared to their bulk counterparts.[149–151] The significant improvement and unique features observed for exfoliated COFs have propelled the development of various strategies for the delamination of COFs. The commonly employed routes include mechanical exfoliation, solvent/liquid-assisted exfoliation, and chemical exfoliation. Solvent-assisted exfoliation is a mild method for exfoliation, espoused for its non-damaging approach. Exploiting the

**Table 2**   Summary of the literature on COF-based chemiresistive $H_2$ sensors

| S. No. | Material | Sensing temp. | $H_2$ conc. | Sensing properties | Response time (s) | Recovery time (s) | Limit of detection (LOD) | Selectivity | Ref. |
|---|---|---|---|---|---|---|---|---|---|
| 1. | eNT COF | 200 °C | 1% | $\Delta R/R_0 = 30.7$ | 4.5 | 3.9 | 0.14% | — | 152 |
| 2. | TpPa-SO$_3$H CONs | 120 °C | 1% | $\Delta R/R_0 = 12 \pm 1$ | $5.5 \pm 1$ | $2.6 \pm 0.5$ | 0.2% | — | 154 |
| 3. | ePd@TpPa-SO$_3$H | 120 °C | 1% | $\Delta R/R_0 = 29 \pm 1$ | 5.3 | 3.1 | 0.2% | $SO_2$, $NO_2$, and $CH_4$ | 156 |
| 4. | Pd@amicPT | RT | 1% | $\Delta R/R_0 = 67.3$ | 5.3 | 3.5 | 0.18% | $NH_3$, $NO_2$, $SO_2$, and CO | 157 |

advantages of exfoliation, our group was the first to report COF-based $H_2$ chemiresistive sensors and has conducted notable work in $H_2$ sensing with COFs. The following provides a discussion on these works.

**3.2.1 Pristine COFs.** Our group reported the first COF-based metal-free chemiresistive $H_2$ gas sensor utilizing naphthalene-1,4,5,8-tetracaboxylic dianhydride (NDA) and tris (4-aminophenyl)amine (TAPA), NDA-TAPA COF (NT COF), as a sensing element.[152] NT COF is synthesized by a solvothermal approach followed by delamination of the COF into a few layers by an acid exfoliation method (Fig. 10a).[153] The process of exfoliation involved vigorous stirring of NT COF in a mixture of solvents consisting of anhydrous acetonitrile, tetrahydrofuran and trifluoroacetic acid (7 : 3 : 2 ratio) at room temperature. The exfoliated NT COF (eNT COF) retained its basic structure, as supported by powder X-ray diffraction (PXRD) patterns and Fourier-transform infrared (FT-IR) studies. Exfoliation to a-few-layers-thick 2D sheets with a thickness of 17–20 nm was confirmed by atomic force microscopy (AFM) analysis. The

eNT COF dispersion, when integrated into the chemiresistor, demonstrated an appreciable sensing response of 30.7 ± 0.26% at 200 °C for 1% $H_2$ with 4.5 ± 0.6/3.9 ± 0.3 s response/recovery times, respectively (Fig. 10b). The sensitivity of eNT COF towards $H_2$ was ascribed to exfoliation, which permitted the effective interaction of $H_2$ with the functional active sites that were previously buried within the interiors of the COF. The colloidal dispersion of eNT COF allowed straightforward device fabrication by simple drop casting, which facilitated the creation of a more uniform and homogeneous sensing film. The eNT COF sensor was used to quantify varying concentrations of $H_2$ gas, ranging from 1 to 0.2%, at 200 °C. The sensing mechanism, elucidated by DFT calculations, suggested an electrostatic interaction between $H_2$ molecules and the carbonyl oxygen (C=O) atoms of the COF, resulting in increased negative charge density on the carbonyl oxygen (Fig. 10c). Unlike SMOs, where the interaction of $H_2$ is with surface-adsorbed oxygen species, here the electrostatic interaction of $H_2$ occurs with functionalities of the COF. In a recent study by our group, a simple and green in situ gas exfoliation method to exfoliate an imine-linked TpPa–$SO_3H$ COF, synthesized from triformylphloroglucinol (Tp) and 2,5-diaminobenzene sulfonic acid (Pa–$SO_3H$) was demonstrated. The approach utilised the catalytic activity of the –$SO_3H$ groups to induce the hydrolysis of ammonia borane (AB), producing $H_2$ gas within the COF layers, which facilitated exfoliation of the COF into covalent organic nanosheets (CONs). CONs realized through this route not only retained the basic structure but exhibited improved photoelectrochemical and photoluminescence properties and good $H_2$ sensing characteristics with a response of 12.5 ± 1%. The response/recovery times were noted as 5.5 ± 1–2.6 ± 0.5s, respectively, at an operating temperature of 120 °C, towards 1% $H_2$ concentration.[154]

**3.2.2 Hybrids of COF decorated with metal ions/nanostructures (MNS@COF).** Functionalizing the COF surface with precious metals like Pd can enhance the material's suitability for $H_2$ sensing applications. It is well-known that COFs are capable of mimicking the role of a surfactant, whereby they restrict aggregation and control the growth of MNPs.[155] In our subsequent study, TpPa–$SO_3H$ COF was used as a support for hybridising Pd NPs.[156] Utilizing a wet impregnation route, a metal–COF hybrid, Pd@TpPa–$SO_3H$ COF, was synthesised. The acidic –$SO_3H$ groups in TpPa–$SO_3H$ COF are considered to play a crucial role in immobilizing the Pd NPs. Post synthesis, Pd@TpPa–$SO_3H$ COF was exfoliated by an acid treatment method (Fig. 11a). Interestingly, the exfoliated Pd@TpPa–$SO_3H$ COF (ePd@TpPa–$SO_3H$) preserved its structural integrity, as supported by PXRD and FTIR studies. Well-dispersed Pd NPs with an average particle size of ~5.6 nm were prominently observed in transmission electron microscopy (TEM) images of ePd@TpPa–$SO_3H$ COF. eTpPa–$SO_3H$ COF exhibited ambiguous behaviour when exposed to 1% $H_2$, at 120 °C. In contrast, ePd@TpPa–$SO_3H$ was found to be sensitive to $H_2$, exhibiting a pronounced decrease in resistance, as quantified by a response of 29 ± 1% with fast response/recovery times of 5.3 ± 0.5/3.1 ± 1 s for 1% $H_2$ (Fig. 11b and c). The optimum working tempera-
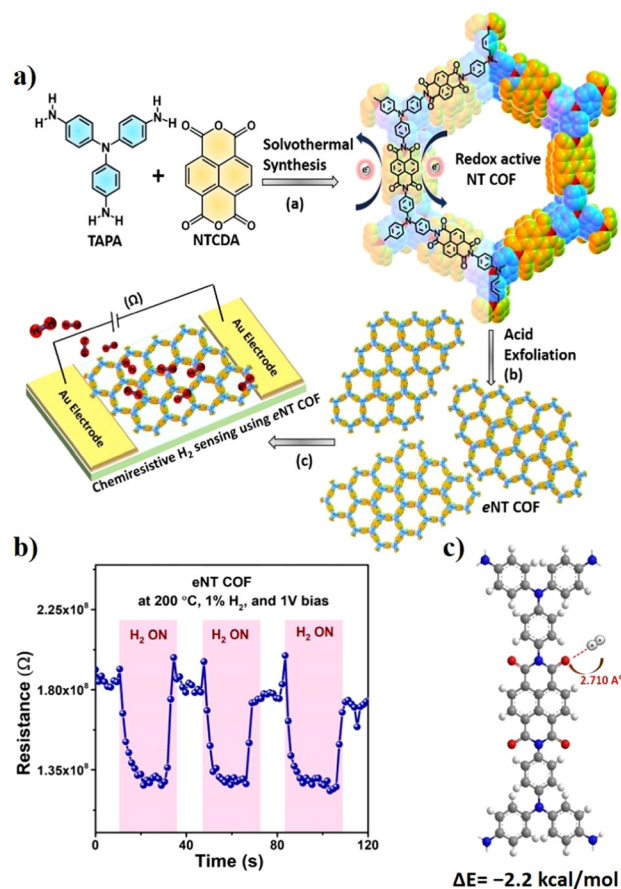


**Fig. 10** (a) Schematic illustration of the structure of the NT COF showing the solvothermal synthesis of the NT COF, acid exfoliation of the NT COF (eNT COF) and a chemiresistive $H_2$ gas sensing device using eNT COF. (b) Response and recovery curve of eNT COF at optimum temperature with 1% $H_2$ concentration. (c) Molecular electrostatic potential plot of the optimized binding site. Reproduced with permission from ref. 152, Royal Society of Chemistry, Copyright@2023.
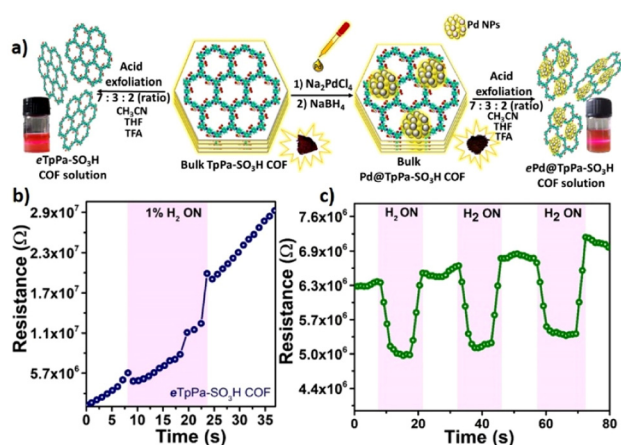
**Fig. 11** (a) Schematic illustration depicting the experimental protocol followed to prepare exfoliated TpPa-SO$_3$H COF and Pd loaded COF; the Tyndal light scattering effect of dispersions of $e$Pd@TpPa-SO$_3$H COF is also shown. (b) H$_2$ gas sensing performance of $e$TpPa-SO$_3$H COF at 80 °C. (c) Response and recovery curve of $e$Pd@TpPa-SO$_3$H COF at optimum temperature with 1% H$_2$ concentration. Reproduced with permission from ref. 156, American Chemical Society, copyright@2023.



**Fig. 12** (a) Schematic illustration of the synthesis of PT COF and Pd@amicPT material; the Tyndal light scattering effect of the dispersion is also shown. (b) H$_2$ gas sensing performance of the Pd@amicPT sensor at optimum temperature, 30 °C, for 1% H$_2$. (c) Effect of concentrations ranging from 0.2 to 1% of H$_2$. Reproduced with permission from ref. 157, Elsevier, copyright@2024.

ture reported for $e$Pd@TpPa–SO$_3$H was 120 °C. $e$Pd@TpPa–SO$_3$H COF represents the first example of an exfoliated metal–COF hybrid integrated into an H$_2$ sensing chemiresistor. Notable sensing characteristics of $e$Pd@TpPa–SO$_3$H COF include its selectivity towards H$_2$, with no cross-sensitivity to relative humidity (75 and 85%) or other interfering gases such as SO$_2$, NO$_2$, and CH$_4$, and long-term stability over 190 days. The sensing mechanism in the $e$Pd@TpPa–SO$_3$H based sensor is attributed to the adsorption–desorption of H$_2$ on catalytic sites facilitated by Pd NPs and the consequent formation of PdH$_x$ species, resulting in noticeable changes in resistance. The study showcased the structural richness of the COF that was retained even after exposure to H$_2$. In other recent work by our group, a rapid H$_2$ sensor operating at room temperature, was reported by employing a redox-active COF, namely a PT COF constructed by polyimidization of pyromellitic dianhydride (PMDA) and tris(4-aminophenyl)amine (TAPA) (Fig. 12a).[157] The PT COF features a bicontinuous donor–acceptor structure and is used as a functional material for energy storage and gas adsorption.[158] Additionally, the structural framework of the PT COF is reductive in nature owing to the presence of the triphenylamine (TPA) moiety. Leveraging the reductive framework, the study demonstrated a simplified methodology to load Pd NPs on the COF, wherein TPA effectively reduced Pd$^{2+}$ ions to Pd$^0$ without the use of conventional reducing agents such as NaBH$_4$. The sites on the framework acted as docking sites for the Pd ions, which eventually transformed into Pd NPs. The Pd NPs decorated the PT COF sensor, referred to as Pd@amicPT, which operated at room temperature (30 °C), with a high response of 67.3% and rapid response–recovery times of 5.3–3.5 s, respectively (Fig. 12b and c). The sensor remained unaffected by relative humidity (8 and 75%) with long-term stability of over 300 days. Furthermore,
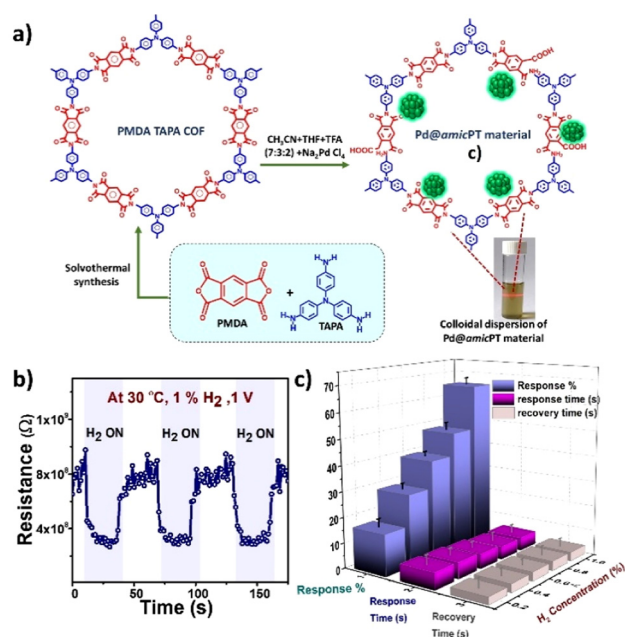
the sensor exhibited appreciable reproducibility, repeatability and selectivity among other gases, including NH$_3$, NO$_2$, SO$_2$, CO. The high sensitivity of the Pd@amicPT sensor at low temperature, such as 30 °C, is attributed to the presence of Pd NPs docked on the COF surface and subsequent formation of PdH$_x$ species upon exposure to H$_2$. The study demonstrated the significant role of the underlying COF framework in immobilizing Pd NPs and in providing an efficient percolation pathway for effective charge transport.

These studies illustrate the significant potential of COFs as emerging materials that can effectively serve as chemiresistive sensing elements for H$_2$. The hybridization of COFs with Pd also offers benefits such as high selectivity and a noticeable improvement in response% and reaction kinetics of the sensor. COFs have yielded promising findings, pushing the boundaries for the effective detection of H$_2$ under ambient conditions, below its flammability limit.

## 4. H$_2$ sensing mechanism: SMO *vs.* porous CFs

Commonly adapted mechanisms for H$_2$ sensing in SMOs and porous CFs are discussed in this section.

### 4.1 H$_2$ sensing mechanism in SMOs

In general, H$_2$ detection by SMO-based sensors is primarily influenced by oxygen (O$_2$) ions, oxygen-deficient sites, and

ions present in the interstitial sites of SMOs, which play a vital role in electrical conductance.[26] Typically, the charge carriers are free electrons ($e^-$) in n-type SMOs and holes ($h^+$) in p-type SMOs. When oxygen, an oxidising molecule from air, adsorbs on the surface of the SMO, it acquires a negative charge by capturing $e^-$ from the conduction band, forming adsorbed oxygen species such as $O_2^-$(ads), $O^-$(ads) and $O^{2-}$(ads) (ads: denotes an adsorption site on the surface); this results in the formation of an electron-depleted region or hole-accumulation region in n- or p-type SMOs, respectively.[159] Variations in electrical conductivity occur when these chemisorbed oxygen species interact with the $H_2$ gas. In most of the n-type SMOs, such as ZnO, $In_2O_3$, and $WO_3$, a redox reaction occurs between $H_2$ and adsorbed oxygen species, producing water and free $e^-$. The produced $e^-$ thins the depletion layer, resulting in a significant decrease in the device resistance, as illustrated in Scheme 7a.[160,161] For a p-type SMO, exposure to $H_2$ removes the holes and increases the resistance (Scheme 7a).[162-164] Under certain circumstances, a direct interaction of $H_2$ with the SMO, resulting in the formation of a metallized region and causing a reduction in resistance, is also reported.[165,166] In either case, the SMO reverts to its original state, and the resistance returns to its initial value when re-exposed to air, implying the reversibility of the interaction and re-adsorption of

oxygen onto the SMO (Scheme 7a). This widely accepted mechanism infers that the effective interaction between $H_2$ and chemisorbed oxygen species critically influences the sensing capability of the SMO-based sensor.

### 4.2 Sensing mechanism in pristine CFs

The plausible $H_2$ sensing mechanism proposed for pristine MOFs in the existing literature is an extrapolation of a similar concept of electron depletion or hole accumulation that occurs in SMOs (Scheme 7b). The changes in resistance are dictated by the type of MOF (n-type or p-type) in addition to interactions between $H_2$ gas and the framework, more specifically with ligands. For instance, in the combined ZIF-8 and ZIF-67 sensor studied by D. Matataguia et al., the chemiresistive response was represented by an increase in the resistance of the material.[100] The response is attributed to the p-type electrical behaviour of the materials and reductive nature of $H_2$. In Co-MOF-I and Co-MOF-II (Co-MOF-74 based sensors), demonstrated by D. K. Nguyen et al., the sensing behaviour of the MOFs is explained using the concept of an electron-depletion mechanism, which involves redox changes in the chemisorbed oxygen species and an interaction with the reducing $H_2$ environment, resulting in a decrease in resistance.[102] An analogous pathway is reported by H. W. Kim et al. for a Zn-
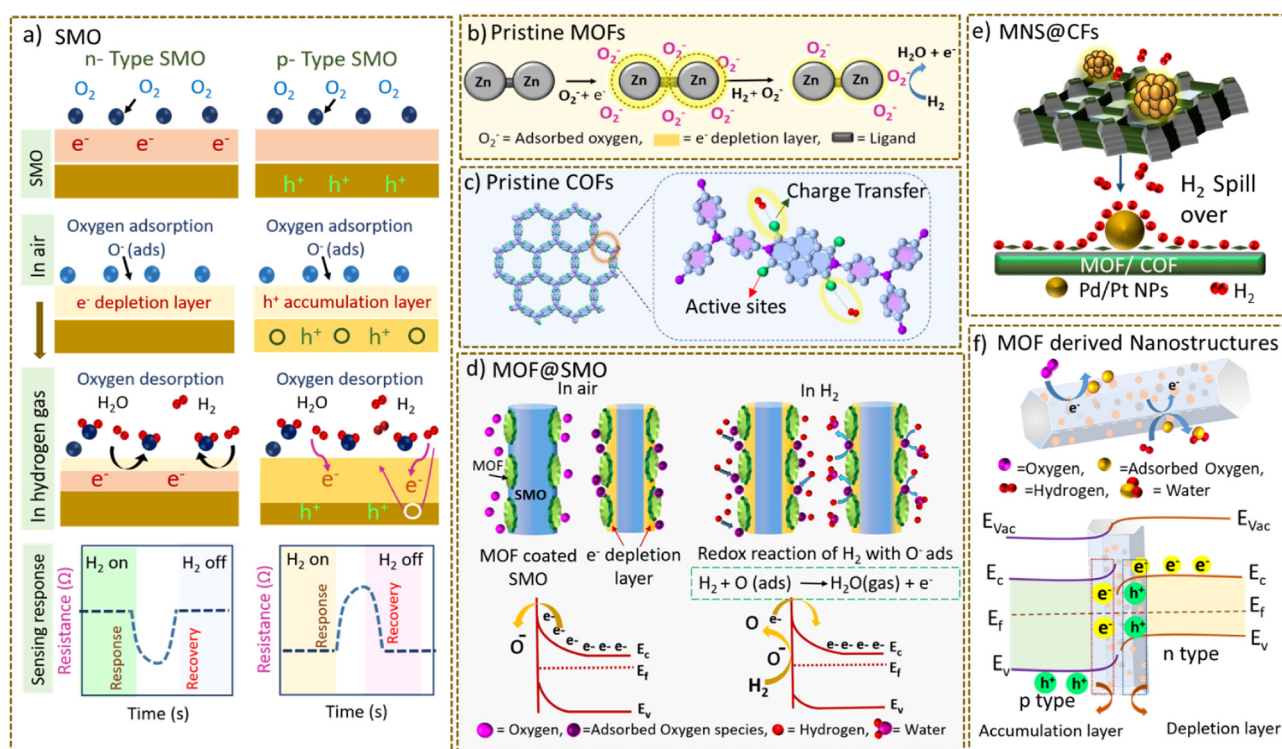


**Scheme 7** Schematic illustration of the sensing mechanism for the detection of $H_2$. (a) In n-type and p-type SMO. The scheme illustrates the corresponding resistance vs. time plot displaying a decrease in n-type SMO and an increase in the resistance in p-type SMO, upon exposure to $H_2$ gas. This figure has been reproduced from ref. 167 with permission from Shodhganga, copyright@2023. (b) $H_2$ sensing mechanism in pristine MOFs. This figure has been reproduced from ref. 101 with permission with modification, Elsevier, copyright@2022. (c) $H_2$ sensing mechanism in pristine COFs. (d) $H_2$ sensing mechanism in SMO@MOF hybrid materials, adapted with permission with modification from ref. 171, Elsevier, copyright@2019. (e) Spill-over effect in metal NP loaded MOF/COF composites. (f) $H_2$ sensing mechanism in MOF-derived materials, adapted with permission with modification from ref. 171, Elsevier, copyright@2019.

BDC-NH$_2$ based sensor, which is known to exhibit n-type behaviour.[101] However, these studies lack substantial experimental evidence and are rather an adaptation of the mechanism followed by SMO MOF-based materials. Therefore, deriving a clear sensing mechanism is difficult and a thorough understanding of the interaction of H$_2$ with pristine MOFs requires further comprehensive studies in this area.

Our understanding of the H$_2$ sensing mechanism in pristine COFs is in the relatively nascent stage, as the field is in the early stages. In pristine COFs, charge transfer interactions between H$_2$ and functional groups present in the structure of the COFs play a determining role in chemiresistive sensing that distinguish COFs from the mechanism that operates in SMOs.[64,103,143–145] For instance, as reported in our study, an electrostatic interaction between H$_2$ and the carbonyl oxygen in eNT COF may be responsible for changes in the resistance of eNT COF, as revealed from DFT calculations. Mulliken charge analysis also indicates charge transfer from the H$_2$ molecule to the oxygen atom of the NDI linker, which results in a chemiresistive response (described in section 3.2.1).[153] Calculations also revealed that the negative charge density on the oxygen atom increased under an electric field, which further strengthened the interaction with H$_2$. It is noteworthy that there is very little focus on the direct use of pristine COFs as H$_2$ sensors; however, there are reports in the literature on other analyte gases such as NO$_2$, NH$_3$, H$_2$S, and VOCs.[63,168–170] All these studies revealed the critical role of functional groups such as the triazine core, imine linkages etc. in the sensing mechanism. A schematic illustrating the interaction of H$_2$ with the functional groups in COFs is shown in Scheme 7c.

### 4.3 Sensing mechanism in hybrid CFs

In the hybrids of SMOs encapsulated by MOFs, the well-defined and highly porous structure of a MOF functions as a molecular sieving layer, which increases the permeability and concentration of the H$_2$ interaction. The pre-concentrated H$_2$ molecules undergo typical redox reactions with the chemisorbed oxygen species, on the SMO surface (described in section 4.1). This process brings about a change in the resistance of the overall sensing material, which is measured as a H$_2$ sensing signal (Scheme 7d).

In composites of Pd@MOF, the permeability and interaction of H$_2$ are primarily governed by three effects: (a) pre-concentration, (b) spill-over, and (c) charge transfer. Pd exhibits a reversible interaction with H$_2$ that makes it particularly beneficial for real-time H$_2$ detection. The pre-concentrated H$_2$ molecules are easily dissociated to hydrogen atoms by the Pd NPs, owing to their high catalytic activity. These dissociated hydrogen atoms then easily migrate (spill over) to the surface of the MOF (Scheme 7e). Notably, Pd@MOF composites exhibit a decrease in resistance when exposed to H$_2$, behaviour that can be attributed to the formation of hydrides, and an associated phase transition from α-PdHx to β-PdHx, as discussed in section 1. The phase change causes a volume expansion, while reducing discontinuities within the Pd nanostructures, thus resulting in effective charge transfer from Pd

to the underlying material and, consequently, lowering the resistance.[116] A similar role of Pd is anticipated in the case of Pd@COF hybrid materials,[157,158] wherein the formation of PdH$_x$ species increases the charge carrier concentration in the material owing to its lower work function compared to Pd. The sensing response is generally produced as a negative sigmoidal curve.

### 4.4 Sensing mechanism in MOF-derived materials

Due to the challenges associated with poor electrical conductivity and charge migration of pristine MOFs, these MOFs have been pyrolyzed at high temperature to obtain nanostructures different from the parent MOF. The MOF-derived nanostructures possess graphitic carbon/a nitrogen-doped carbon network and metal oxide dispersed throughout the matrix.[133] The graphitic carbon provides facile charge transport pathways while the derived metal oxide nanostructures possess abundant oxygen adsorption sites/vacancies in addition to multi-component n–n/p–n heterojunctions (Scheme 7d).[134] These materials have shown rapid charge migration and improved H$_2$ interactions. This is followed by the redox reactions occurring at the surface of the MOF-derived metal oxide analogous to the phenomenon occurring in the presence of SMOs. In summary, improved charge distribution due to synergistic interactions and the subsequent surface redox reaction with H$_2$ lead to the sensing of H$_2$ in the case of MOF-derived materials.[134]

Taken together with the discussion on H$_2$ sensing, MOFs and COFs exhibit different sensing mechanisms towards H$_2$ as compared to that of SMOs. It should be noted that the highly porous nature, large surface area, and diverse functionalities resulting from a variety of linkers in MOFs/COFs could be additional gears that might provide a new mechanism of H$_2$ sensing. Although limited studies exist on MOFs that follow the electron depletion/accumulation concept, we presume that in pristine MOFs and COFs, sensing is primarily governed by functional groups and linkers, as well as metal clusters in the case of MOFs. When examining the sensing mechanisms of MOFs for analytes other than H$_2$, there is a clear indication that the metal nodes present in MOFs can coordinate with the analytes, enabling selective and sensitive detection of gases.[53,60,64] In metal NP-loaded MOF and COF hybrids, similar behaviour is expected from both materials, with the NPs playing a crucial role in facilitating charge transfer.

## 5. Conclusion and future perspectives

MOFs/COFs belonging to the CF family are demonstrated to be promising materials for next-generation chemiresistive H$_2$ gas sensors through recent examples. Owing to their beneficial structural features, such as rich pore chemistry, high surface area, and well-defined active sites, these materials provide wide opportunities for exploration. While MOFs and their hybrids have been relatively well-explored for H$_2$ sensing, the

exploration of COFs in this area represents a promising venture that still needs to be fully exploited. In our opinion, COFs carry greater promise as materials for $H_2$ sensing due to their rich functional diversity. COFs are constructed with linkages, such as boronic esters, imines, imides, hydrazones, azines, triazines, and polar groups (C=O, NH, S=O), that can act as active sites for reversible interactions with the analyte. Unlike MOFs, where charge transport relies on hopping transport or "guest-promoted" mechanisms, COFs offer more efficient charge transport, arising from the framework itself, due to enhanced in-plane/interplanar charge transport routes. This makes COFs particularly promising for advanced $H_2$ sensing applications. However, CFs exhibit certain limitations that cannot be overlooked and must be addressed to enhance their performance as sensors:

(i) Limited detection range: CFs are generally effective at detecting higher analyte concentrations, typically above 0.1 ppm, but struggle to achieve sensitivity at lower trace levels.

(ii) Long-term drift: some CF-based sensors experience long-term drift in baseline resistance, affecting their performance and reliability over time.

(iii) Difficulty in processability: the large-scale green synthesis of CFs is not straightforward given control of their long-range-order growth. Moreover, device fabrication is a cumbersome process, as most CF samples exist as bulk materials or powders, making solution processability difficult.

Chemiresistors based on SMOs and CFs complement each other with respect to their $H_2$ sensing characteristics (Fig. 13). SMOs have the ability to detect $H_2$ at low concentrations (in ppm levels) with good stability (less drift in baseline over time), making them ideal for the trace level detection of $H_2$. However, they require high temperatures ($\geq$300 °C), saturation of signals at higher concentrations and the presence of oxygen. Additionally, SMOs suffer from low selectivity, particularly with gases such as CO and $SO_2$. On the other hand, CF sensors work very well for detecting gases at higher concentrations (0.2–5%), with excellent selectivity. They can operate efficiently under inert conditions as the sensing mechanism is different from that of SMOs. Importantly, the CF-based sensors have the ability to work at moderate temperatures (low temperature range from room temperature to 250 °C), making them suitable candidates for the development of energy-saving chemiresistive gas sensors. Furthermore, most of the reported CF-based sensors exhibited good stability towards humidity. However, the gas sensing data discussed in this review clearly suggest that baseline drift over time is a common phenomenon in these classes of materials. Though CFs do not appear suitable for trace level $H_2$ detection, their ability to handle higher concentrations, where semi-conductor oxides may fail, makes them a valuable complement in comprehensive gas sensing systems.

In order to design efficient $H_2$ sensors based on pristine CFs, the synthetic design strategies should aim to create
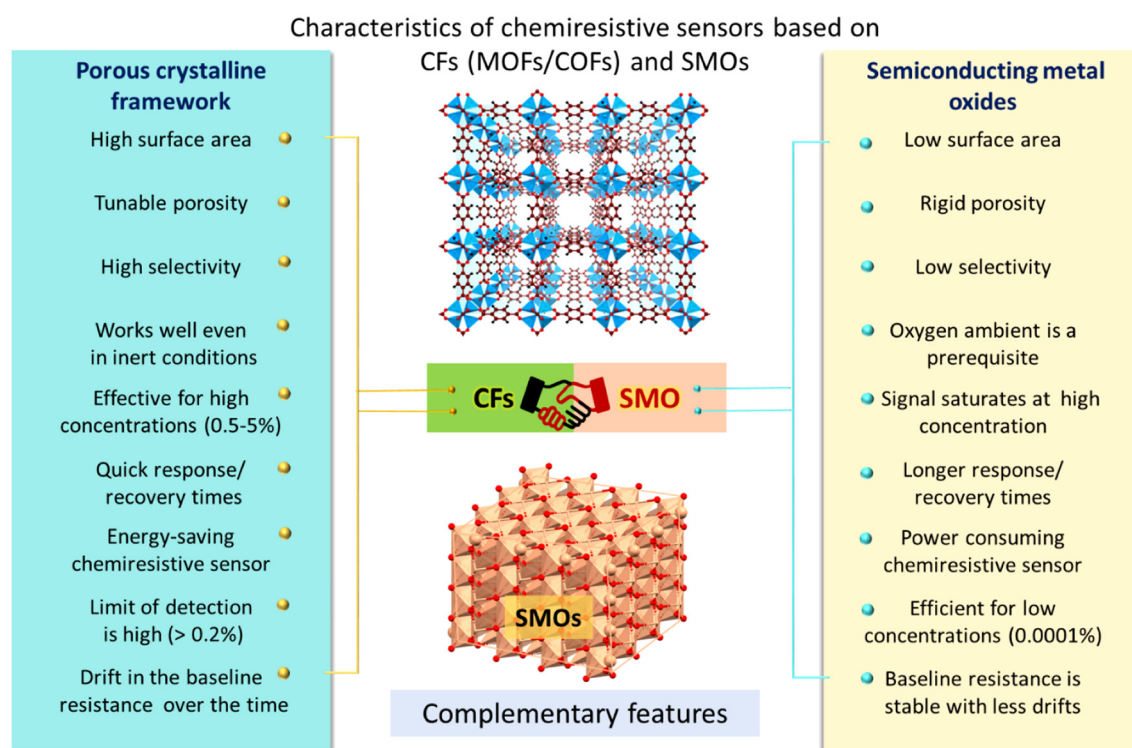


**Fig. 13** Schematic representation of the characteristic features of CFs and SMOs to complement each other in developing efficient hybrid materials for chemiresistive sensing devices.

notable active sites for $H_2$ interactions. These include functional groups in the organic linker and open metal centers in the secondary building units. Additionally, it is crucial that the interactions with $H_2$ are efficiently converted into measurable signals.[172] To achieve this, the framework must possess facile electron-conducting pathways. The incorporation of redox-active linkers (tetrathiafulvalene (TTF) based linkers, metal-bis(dithiolene), naphthalene diimide (NDI) based linkers and quinone-based linkers) can significantly enhance charge transfer properties in CFs.[173,174] Additionally, in MOFs, the use of transition metal nodes with partially filled d-orbitals (*e.g.*, Fe or Co) has shown promise for creating MOFs with tunable band gaps, contributing to their semiconducting nature.[175] Furthermore, effective signal transduction between particles is critical for the overall performance of the sensing material. Therefore, the utilization of methods such as layer-by-layer assembly, electrophoretic deposition, and spin coating should be an integral part of the device fabrication process.[176]

Considering the versatility and adaptability of MOFs and COFs, we foresee that the challenges posed by individual materials in chemiresistive sensing can be addressed through hybridization with other materials to form composites, such as CFs hybridized with SMOs (CF@SMO), MOFs with other MOFs (MOF@MOF), MOFs with COFs (MOF@COF), COFs with MOFs (COF@MOF) or employing conducting MOFs/COFs. The prospects for some of these systems in realizing high-performance sensing are discussed below.

### 5.1 SMO–CF hybrids

Upon reviewing the strengths and limitations of CFs and SMOs, we recognize their potential for synergistic complementarity. Modifying CFs with SMOs could enhance various sensor parameters. The approach involves hybridizing SMOs with CFs to form composites like SMO@MOFs or SMO@COFs, leveraging the strengths of each material. This strategy anticipates that the hybrid composite material could offer improved properties such as broader detection ranges with better sensitivity. For example, in a study, our group demonstrated the assembly of cobalt-imidazole based ZIF-67 MOF onto $SnO_2$ nanoparticles to create $SnO_2$@ZIF-67 material.[177] The ZIF-67 MOF is effective at capturing $CO_2$. Coating $SnO_2$ with ZIF-67 significantly boosted the sensitivity of $SnO_2$ towards $CO_2$ at relatively low temperature. The response of $SnO_2$@ZIF-67 is reported to be 16.5% at 205 °C for 5% of $CO_2$, which is one of the highest values recorded for a $SnO_2$-based sensor. The response represents a 3-fold increase compared to pristine $SnO_2$ under the same conditions. The study is a demonstration of the superior performance of SMO@MOF hybrid materials and provides ways to design novel sensors for $H_2$ by utilizing the same strategy.

Recent research has highlighted the effective use of 2D materials having p–n heterojunctions in gas sensing applications.[178] By carefully selecting p–n junction configurations composed of MOFs/COFs and SMOs, researchers can tailor their properties to achieve selectivity and robust sensing characteristics. For example, Andre *et al.* developed a p–n het-

erojunction using n-type $In_2O_3$ and p-type reduced graphene oxide (rGO), which exhibited an excellent sensing performance for $NH_3$.[179] We expect that creating such heterojunctions with COFs/MOFs might substantially enhance the $H_2$ sensing abilities.

### 5.2 MOF@COF and COF@MOF composites

Current research has focused on the integration of MOFs with MOFs and MOFs with COFs, which have exciting electro-chemical, biosensing, and chemiresistive sensor applications.[66,180,181] For example, Cho *et al.* integrated a 2D MOF (Ni-HHTP) with a 3D MOF (UiO-66-$NH_2$), which showed excellent porosity, conductivity, and new interfacial properties.[182] This hybrid MOF was successfully employed for the chemiresistive sensing of toxic $H_2S$ gas, achieving enhanced sensitivity with a remarkably low detection limit of 1.4 ppb. While such approaches have not yet been explored for $H_2$ sensing, further research in this direction holds promise for enhanced sensing capabilities.

### 5.3 Conducting MOFs/COFs

A notable number of conducting MOFs and COFs have been documented in the literature, offering their versatility across various applications,[183] including chemiresistive sensing.[67] These conductive CF sensors operate effectively at room temperature and exhibit impressive selectivity and sensitivity towards low-concentration gases. A study by Yao *et al.* demonstrated the effectiveness of a conducting MOF chemiresistor, $Cu_3$(HHTP)(THQ), utilizing conductive organic linkages, HHTP (2,3,6,7,10,11-hexahydrotriphenylene) and THQ (tetrahydroxy-1,4-quinone), which showed excellent $NH_3$ detection capabilities under ambient conditions.[184] In contrast, research on conducting COF sensors remains relatively limited. Meng *et al.* reported a prominent example, COF-DC-8, of a 2D-COF employing 2,3,9,10,16,17,23,24-octa-amino phthalocyanine nickel(II) and pyrene-4,5,9,10-tetraone linkages, signifying superior detection of various gases such as $NH_3$, $H_2S$, NO, and $NO_2$ at low concentrations (ppb level) at room temperature.[63] However, reports based on $H_2$ sensors are very limited in this direction. Considering initial studies in this area and promising prospects for future research, we believe that MOF/COF-based chemiresistors have great potential to surpass state-of-the-art $H_2$ sensing characteristics. The area also provides enough opportunities for theoretical and experimental researchers to understand the interactions between $H_2$ and MOF/COF linkers, which are responsible for $H_2$ sensing. This may enable the rational design of MOFs/COFs with suitable linkers to realize enhanced sensing performance. Furthermore, the molecular level design of CFs with redox-active linkers with functional groups such as imine, phenazine, carbonyl *etc.* that have the ability to interact with $H_2$ are particularly beneficial for $H_2$ sensing materials. Furthermore, interactive guest molecules and the incorporation of mixed-valence systems are crucial for optimizing the structure and enhancing the sensing capabilities of CF materials. Thus, the proper amalgamation of synthetic chemists, materials che-

mists, device physicists and theoreticians may further enhance this area and lead to the development of effective porous CF-based $H_2$ sensors.

## Author contributions

M.E.D. and N.T. contributed equally. The manuscript was written through contributions of all authors. All authors have given approval to the final version of the manuscript.

## Data availability

No primary research results, software or code have been included and no new data were generated or analysed as part of this review.

## Conflicts of interest

There are no conflicts to declare.

## Acknowledgements

## References

1 A. Mehtab, S. A. Ali, I. Sadiq, S. Shaheen, H. Khan, M. Fazil, N. A. Pandit, F. Naaz and T. Ahmad, *ACS Sustainable Resour. Manage.*, 2024, **1**, 604–620.

2 D. Guan, B. Wang, J. Zhang, R. Shi, K. Jiao, L. Li, Y. Wang, B. Xie, Q. Zhang, J. Yu, Y. Zhu, Z. Shao and M. Ni, *Energy Environ. Sci.*, 2023, **16**, 4926–4943.

3 T. T. Le, P. Sharma, B. J. Bora, V. D. Tran, T. H. Truong, H. C. Le and P. Q. P. Nguyen, *Int. J. Hydrogen Energy*, 2024, **54**, 791–816.

4 A. Midilli and I. Dincer, *Int. J. Hydrogen Energy*, 2008, **33**, 4209–4222.

5 P. A. Le, V. D. Trung, P. L. Nguyen, T. V. Bac Phung, J. Natsuki and T. Natsuki, *RSC Adv.*, 2023, **13**, 28262–28287.

6 V. R. Bakuru, M. E. Dmello and S. B. Kalidindi, *ChemPhysChem*, 2019, **20**, 1177–1215.

7 M. Yue, H. Lambert, E. Pahon, R. Roche, S. Jemei and D. Hissel, *Renewable Sustainable Energy Rev.*, 2021, **146**, 111180.

8 S. Evro, B. A. Oni and O. S. Tomomewo, *Int. J. Hydrogen Energy*, 2024, **78**, 1449–1467.

9 G. Nicoletti, N. Arcuri, G. Nicoletti and R. Bruno, *Energy Convers. Manage.*, 2015, **89**, 205–213.

10 A. Roy and S. Pramanik, *Int. J. Hydrogen Energy*, 2024, **49**, 792–821.

11 D. Hu, P. Gao, Z. Cheng, Y. Shen, R. He, F. Yi, M. Lu, J. Wang and S. Liu, *Energy Fuels*, 2024, **38**, 4803–4835.

12 Q. Hassan, I. Azzawi, A. Zuhair and H. Salman, *Sustainability*, 2023, **15**, 1–26.

13 L. Guo, J. Su, Z. Wang, J. Shi, X. Guan, W. Cao and Z. Ou, *Int. J. Hydrogen Energy*, 2024, **51**, 1055–1078.

14 S. Foorginezhad, M. Mohseni-Dargah, Z. Falahati, R. Abbassi, A. Razmjou and M. Asadnia, *J. Power Sources*, 2021, **489**, 229450.

15 T. M. Swager, T. N. Pioch, H. Feng, H. M. Bergman, S.-X. L. Luo and J. J. I. I. Valenza, *ACS Sens.*, 2024, **9**, 2205–2227.

16 S. K. Arya, S. Krishnan, H. Silva, S. Jean and S. Bhansali, *Analyst*, 2012, **137**, 2743–2756.

17 B. K. S. Reddy and P. H. Borse, *J. Electrochem. Soc.*, 2021, **168**, 057521.

18 W. T. Koo, H. J. Cho, D. H. Kim, Y. H. Kim, H. Shin, R. M. Penner and I. D. Kim, *ACS Nano*, 2020, **14**, 14284–14322.

19 T. Seiyama, K. Fujiishi, M. Nagatani and A. Kato, *J. Soc. Chem. Ind., Jpn.*, 1963, **66**, 652–655.

20 B. W. H. Brattain and J. Bardeent, *Am. Teleph. Telegr. Co.*, 1952, **32**, 1–41.

21 G. Heiland, *Z. Phys.*, 1954, **138**, 459–464.

22 N. Taguchi, *US Pat*, 3631436, 1971.

23 G. Neri, *Chemosensors*, 2015, **3**, 1–20.

24 H. Wohltjen, W. R. Barger, A. W. Snow and N. L. Jarvis, *IEEE Trans. Electron Devices*, 1985, **32**, 1170–1174.

25 H. Gu, Z. Wang and Y. Hu, *Sensors*, 2012, **12**, 5517–5550.

26 M. B. Rahmani, M. H. Yaacob and Y. M. Sabri, *Sens. Actuators, B*, 2017, **251**, 57–64.

27 C. Kuru, C. Choi, A. Kargar, D. Choi, Y. J. Kim, C. H. Liu, S. Yavuz and S. Jin, *Adv. Sci.*, 2015, **2**, 1–5.

28 L. Gao, Y. Tian, A. Hussain, Y. Guan and G. Xu, *Anal. Bioanal. Chem.*, 2024, **416**, 3697–3715.

29 P. Dariyal, S. Sharma, S. Chauhan, P. Singh and S. R. Dhakate, *Nanoscale Adv.*, 2021, **3**, 6514–6544.

30 E. Llobet, *Sens. Actuators, B*, 2013, **179**, 32–45.

31 A. Ilnicka and J. P. Lukaszewicz, *Processes*, 2020, **8**, 633.

32 E. Kowalska, E. Czerwosz, R. Diduszko, A. Kaminska and M. Danila, *Sens. Actuators, A*, 2013, **203**, 434–440.

33 Q. Li, L. Wang, A. Xiao, L. Zhu and Z. Yang, *Int. J. Hydrogen Energy*, DOI: **10.1016/j.ijhydene.2024.01.001**.

34 I. Darmadi, F. A. A. Nugroho and C. Langhammer, *ACS Sens.*, 2020, **5**, 3306–3327.

35 C. Wadell, F. A. A. Nugroho, E. Lidström, B. Iandolo, J. B. Wagner and C. Langhammer, *Nano Lett.*, 2015, **15**, 3563–3570.

36 A. Mirzaei, H. R. Yousefi, F. Falsafi, M. Bonyani, J. H. Lee, J. H. Kim, H. W. Kim and S. S. Kim, *Int. J. Hydrogen Energy*, 2019, **44**, 20552–20571.

37 M. Tiemann, *Chem. – Eur. J.*, 2007, **13**, 8376–8388.

38 P. M. Bulemo and J. Y. Cheong, *ACS Appl. Nano Mater.*, 2023, **6**, 1027–1049.

39 J. Zhang, Z. Qin, D. Zeng and C. Xie, *Phys. Chem. Chem. Phys.*, 2017, **19**, 6313–6329.

40 A. Sharma, S. B. Eadi, H. Noothalapati, M. Otyepka, H. D. Lee and K. Jayaramulu, *Chem. Soc. Rev.*, 2024, **53**, 2530–2577.

41 J. Ha, J. H. Lee and H. R. Moon, *Chem. Front.*, 2020, **7**, 12–27.

42 D. J. Tranchemontagne, J. L. Mendoza-Cortés, M. O'Keeffe and O. M. Yaghi, *Chem. Soc. Rev.*, 2009, **38**, 1257–1283.

43 https://hdl.handle.net/10603/426879.

44 H. Ghasempour, K. Y. Wang, J. A. Powell, F. Zarekarizi, X. L. Lv, A. Morsali and H. Zhou, *Coord. Chem. Rev.*, 2021, **426**, 213542.

45 A. P. Côté, A. I. Benin, N. W. Ockwig, M. O'Keeffe, A. J. Matzger and O. M. Yaghi, *Science*, 2005, **310**, 1166–1170.

46 C. S. Diercks and O. M. Yaghi, *Science*, 2017, **355**, eaal1585.

47 N. Huang, P. Wang and D. Jiang, *Nat. Rev. Mater.*, 2016, **1**, 16068.

48 H. R. Abuzeid, A. F. M. El-Mahdy and S. W. Kuo, *Giant*, 2021, **6**, 100054.

49 R. K. Parashar, P. Jash, M. Zharnikov and P. C. Mondal, *Angew. Chem., Int. Ed.*, 2024, **63**, e202317413.

50 L. S. Xie, G. Skorupskii and M. Dincă, *Chem. Rev.*, 2020, **120**, 8536–8580.

51 M. Ko, L. Mendecki and K. A. Mirica, *Chem. Commun.*, 2018, **54**, 7873–7891.

52 R. Saha and C. J. Gomez Garcia, *Chem. Soc. Rev.*, 2024, 9490–9559.

53 V. Rubio-Giménez, N. Almora-Barrios, G. Escorcia-Ariza, M. Galbiati, M. Sessolo, S. Tatay and C. Martí-Gastaldo, *Angew. Chemie*, 2018, **130**, 15306–15310.

54 M. Souto and D. F. Perepichka, *J. Mater. Chem. C*, 2021, **9**, 10668–10676.

55 R. Gutzler and D. F. Perepichka, *J. Am. Chem. Soc.*, 2013, **135**, 16585–16594.

56 M. R. Rao, Y. Fang, S. De Feyter and D. F. Perepichka, *J. Am. Chem. Soc.*, 2017, **139**, 2421–2427.

57 M. Yu, R. Dong and X. Feng, *J. Am. Chem. Soc.*, 2020, **142**, 12903–12915.

58 D. M. D'Alessandro, *Chem. Commun.*, 2016, **52**, 8957–8971.

59 S. Lin, P. M. Usov and A. J. Morris, *Chem. Commun.*, 2018, **54**, 6965–6974.

60 M. G. Campbell, D. Sheberla, S. F. Liu, T. M. Swager and M. Dincə, *Angew. Chem., Int. Ed.*, 2015, **54**, 4349–4352.

61 E. X. Chen, H. R. Fu, R. Lin, Y. X. Tan and J. Zhang, *ACS Appl. Mater. Interfaces*, 2014, **6**, 22871–22875.

62 L. M. Tao, F. Niu, D. Zhang, T. M. Wang and Q. H. Wang, *New J. Chem.*, 2014, **38**, 2774–2777.

63 Z. Meng, R. M. Stolz and K. A. Mirica, *J. Am. Chem. Soc.*, 2019, **141**, 11929–11937.

64 W.-T. Koo, J.-S. Jang and I.-D. Kim, *Chem*, 2019, **5**, 1938–1963.

65 J. D. Bhaliya, V. R. Shah, G. Patel and K. Deshmukh, *J. Inorg. Organomet. Polym.*, 2023, **33**, 1453–1494.

66 C. Park, J. W. Baek, E. Shin and I. Kim, *ACS Nanosci.*, 2023, **3**, 353–374.

67 A. Sharma, S. B. Eadi, H. Noothalapati, M. Otyepka, H. D. Lee and K. Jayaramulu, *Chem. Soc. Rev.*, 2024, **53**, 2530–2577.

68 A. Mei, Z. Yang, M. Zhou, W. Jin, Y. Liu and W. Chen, *Anal. Sens.*, 2024, **4**, e202300078.

69 M. Zhou, Y. Li and G. Xu, *TrAC, Trends Anal. Chem.*, 2024, **174**, 117679.

70 M. Kim, M. Pander and H. R. Moon, *ACS Appl. Electron. Mater.*, 2024, **6**, 3024–3038.

71 G. H. Pham and C. Z. Dinu, *RSC Sustainability*, 2023, **1**, 1125–1149.

72 Y.-M. Jo, Y. K. Jo, J.-H. Lee, H. W. Jang, I.-S. Hwang and D. J. Yoo, *Adv. Mater.*, 2023, **35**, 2206842.

73 H. Wei, H. Zhang, B. Song, K. Yuan, H. Xiao, Y. Cao and Q. Cao, *Int. J. Environ. Res. Public Health*, 2023, **20**, 4388–4401.

74 H. Yuan, N. Li, W. Fan, H. Cai and D. Zhao, *Adv. Sci.*, 2022, **9**, 1–27.

75 Ankit, N. Saini, H. Pandey and K. Pandey, *Macromol. Symp.*, 2024, **413**, 2300058.

76 N. Garg, A. Deep and A. L. Sharma, *Coord. Chem. Rev.*, 2021, **445**, 214073.

77 A. Chidambaram and K. C. Stylianou, *Inorg. Chem. Front.*, 2018, **5**, 979–998.

78 H. Y. Li, S. N. Zhao, S. Q. Zang and J. Li, *Chem. Soc. Rev.*, 2020, **49**, 6364–6401.

79 A. Melillo, A. Franconetti, M. Alvaro, B. Ferrer and H. Garcia, *Chem. – Eur. J.*, 2023, **29**, e202202625.

80 V. Zeleňák and I. Saldan, *Nanomaterials*, 2021, **11**, 1638.

81 Z. Meng and K. A. Mirica, *Chem. Soc. Rev.*, 2021, **50**, 13498–13558.

82 L. Sun, M. G. Campbell and M. Dincə, *Angew. Chem., Int. Ed.*, 2016, **55**, 3566–3579.

83 R. Saha, K. Gupta and C. J. Gómez García, *Cryst. Growth Des.*, 2024, **24**, 2235–2265.

84 S. G. Ibrahim and A. U. Ubale, *J. Mol. Struct.*, 2014, **1076**, 291–298.

85 G. Givaja, P. Amo-Ochoa, C. J. Gómez-García and F. Zamora, *Chem. Soc. Rev.*, 2012, **41**, 115–147.

86 J. F. Fennell, S. F. Liu, J. M. Azzarelli, J. G. Weis, S. Rochat, K. A. Mirica, J. B. Ravnsbæk and T. M. Swager, *Angew. Chem., Int. Ed.*, 2016, **55**, 1266–1281.

87 M. A. Franco, P. P. Conti, R. S. Andre and D. S. Correa, *Sens. Actuators Rep.*, 2022, **4**, 100100.

88 R. Tang, Y. Shi, Z. Hou and L. Wei, *Sensors*, 2017, **17**, 882–897.

89 N. Le Hung, E. Ahn, S. Park, H. Jung, H. Kim, S.-K. Hong, D. Kim and C. Hwang, *J. Vac. Sci. Technol., A*, 2009, **27**, 1347–1351.

90 F. Rumiche, H. H. Wang and J. E. Indacochea, *Sens. Actuators, B*, 2012, **163**, 97–106.

91 K. Chikkadi, M. Muoth, W. Liu, V. Maiwald and C. Hierold, *Sens. Actuators, B*, 2014, **196**, 682–690.

92 A. Shrivastava and V. Gupta, *Chron. Young Sci.*, 2011, **2**, 21.

93 R. Kumar, R. N. Jenjeti and S. Sampath, *ACS Sens.*, 2020, **5**, 404–411.

94 F. Gu, M. Di, D. Han, S. Hong and Z. Wang, *ACS Sens.*, 2020, **5**, 2611–2619.

95 J. Burgués, J. M. Jiménez-Soto and S. Marco, *Anal. Chim. Acta*, 2018, **1013**, 13–25.

96 M. Drobek, J. H. Kim, M. Bechelany, C. Vallicari, A. Julbe and S. S. Kim, *ACS Appl. Mater. Interfaces*, 2016, **8**, 8323–8328.

97 N. Stock and S. Biswas, *Chem. Rev.*, 2012, **112**(2), 933–969.

98 W.-J. Li, M. Tu, R. Cao and R. A. Fischer, *J. Mater. Chem. A*, 2016, **4**, 12356–12369.

99 M. Rivera-Torrente, L. D. B. Mandemaker, M. Filez, G. Delen, B. Seoane, F. Meirer and B. M. Weckhuysen, *Chem. Soc. Rev.*, 2020, **49**, 6694–6732.

100 D. Matatagui, A. Sainz-Vidal, I. Gràcia, E. Figueras, C. Cané and J. M. Saniger, *Sens. Actuators, B*, 2018, **274**, 601–608.

101 D. H. Yang, T. T. T. Nguyen, S. T. Navale, L. H. T. Nguyen, Y. T. Dang, N. X. D. Mai, T. B. Phan, J.-Y. Kim, T. L. H. Doan, S. S. Kim and H. W. Kim, *Sens. Actuators, B*, 2022, **368**, 132120.

102 D. K. Nguyen, J. H. Lee, T. L. H. Doan, T. B. Nguyen, S. Park, S. S. Kim and B. T. Phan, *Appl. Surf. Sci.*, 2020, **523**, 146487.

103 R. Zhang, L. Lu, Y. Chang and M. Liu, *J. Hazard. Mater.*, 2022, **429**, 128321.

104 Y. Wang and D. Zhao, *Cryst. Growth Des.*, 2017, **17**, 2291–2308.

105 C. Zhang, R. P. Lively, K. Zhang, J. R. Johnson, O. Karvan and W. J. Koros, *J. Phys. Chem. Lett.*, 2012, **3**, 2130–2134.

106 Q. Ke, Y. Duan, Y. Ji, D. Zhao, H. Zhang, C. Duan, L. Li and Y. Wei, *J. Chem. Eng. Data*, 2021, **66**, 3483–3492.

107 D. Peralta, G. Chaplais, A. Simon-Masseron, K. Barthelet, C. Chizallet, A. A. Quoineaud and G. D. Pirngruber, *J. Am. Chem. Soc.*, 2012, **134**, 8115–8126.

108 A. Huang, Q. Liu, N. Wang and Y. Zhu, *J. Am. Chem. Soc.*, 2014, **136**, 14686–14689.

109 Y. Pan, B. Wang and Z. Lai, *J. Membr. Sci.*, 2012, **421–422**, 292–298.

110 C. W. Kung, A. E. Platero-Prats, R. J. Drout, J. Kang, T. C. Wang, C. O. Audu, M. C. Hersam, K. W. Chapman, O. K. Farha and J. T. Hupp, *ACS Appl. Mater. Interfaces*, 2018, **10**, 30532–30540.

111 Z. Wen, L. Zhu, Z. Zhang and Z. Ye, *Sens. Actuators, B*, 2015, **208**, 112–121.

112 H. Yue, Z. Shi, Q. Wang, Z. Cao, H. Dong, Y. Qiao, Y. Yin and S. Yang, *ACS Appl. Mater. Interfaces*, 2014, **6**, 17067–17074.

113 T. Zhou, Y. Sang, X. Wang, C. Wu, D. Zeng and C. Xie, *Sens. Actuators, B*, 2018, **258**, 1099–1106.

114 A. I. Khudiar, A. K. Elttayef, M. K. Khalaf and A. M. Oufi, *Mater. Res. Express*, 2020, **6**, 126450.

115 R. Lv, Q. Zhang, W. Wang, Y. Lin and S. Zhang, *Sensors*, 2021, **21**, 4069.

116 T. B. Flanagan and W. A. Oates, *Annu. Rev. Mater. Sci.*, 1991, **21**, 269–304.

117 W. T. Koo, S. Qiao, A. F. Ogata, G. Jha, J. S. Jang, V. T. Chen, I. D. Kim and R. M. Penner, *ACS Nano*, 2017, **11**, 9276–9285.

118 S. Fardindoost, S. Hatamie, A. I. Zad and F. R. Astaraei, *Nanotechnology*, 2018, **29**, 015501.

119 M. Weber, J. H. Kim, J. H. Lee, J. Y. Kim, I. Iatsunskyi, E. Coy, M. Drobek, A. Julbe, M. Bechelany and S. S. Kim, *ACS Appl. Mater. Interfaces*, 2018, **10**, 34765–34773.

120 B. Xie, B. Ding, P. Mao, Y. Wang, Y. Liu, M. Chen, C. Zhou, H. min Wen, S. Xia, M. Han, R. E. Palmer, G. Wang and J. Hu, *Small*, 2022, **18**, 1–13.

121 M. K. Smith, K. E. Jensen, P. A. Pivak and K. A. Mirica, *Chem. Mater.*, 2016, **28**, 5264–5268.

122 M. G. Campbell, S. F. Liu, T. M. Swager and M. Dincă, *J. Am. Chem. Soc.*, 2015, **137**, 13780–13783.

123 D. M. D'Alessandro, *Chem. Commun.*, 2016, **52**, 8957–8971.

124 H. Feng, J. Wang, Z. Tong and H.-Y. Qu, *Chem. Eng. J.*, 2022, **442**, 136158.

125 K. S. Pedersen, P. Perlepe, M. L. Aubrey, D. N. Woodruff, S. E. Reyes-Lillo, A. Reinholdt, L. Voigt, K. Li, K. Borup, M. Rouzières, D. Samohvalov, F. Wilhelm, A. Rogalev, J. B. Neaton, J. R. Long and R. Clérac, *Nat. Chem.*, 2018, **10**, 1056–1061.

126 M. E. Dmello, R. C. Sahoo, R. Raghunathan, H. S. S. R. Matte, P. Yadav, G. V. Shanbhag and S. B. Kalidindi, *Int. J. Hydrogen Energy*, 2022, **47**, 9477–9483.

127 X. Liu, G. Verma, Z. Chen, B. Hu, Q. Huang, H. Yang, S. Ma and X. Wang, *The Innovation*, 2022, **3**, 100281.

128 N. Cui, K. Bi, W. Sun, Q. Wu, Y. Li, T. Xu, B. Lv and S. Zhang, *Catalysts*, 2021, **11**, 1–12.

129 J. Ren, Y. Huang, H. Zhu, B. Zhang, H. Zhu, S. Shen, G. Tan, F. Wu, H. He, S. Lan, X. Xia and Q. Liu, *Carbon Energy*, 2020, **2**, 176–202.

130 C. Montoro, J.-Y. Kim, A. Mirzaei, J.-H. Lee, S. Sayegh, E. Makhoul, I. Iatsunskyi, E. Coy, M. Bechelany, H. W. Kim and S. S. Kim, *Composites, Part B*, 2024, **283**, 111637.

131 J. Lin, W. Ho, X. Qin, C.-F. Leung, V. K.-M. Au and S.-c. Lee, *Small*, 2022, **18**, 2105484.

132 A. Sharma, K. Karuppasamy, D. Vikraman, Y. Cho, K. Adaikalam, J. G. Korvink, H. S. Kim and B. Sharma, *ACS Appl. Mater. Interfaces*, 2022, **14**, 44516–44526.

133 S. Zhou, J. Ji, T. Qiu, L. Wang, W. Ni, S. Li, W. Yan, M. Ling and C. Liang, *Inorg. Chem. Front.*, 2022, **9**, 599–606.

134 M. E. Dmello, S. Vishwanathan, V. R. Bakuru, G. V. Shanbhag and S. B. Kalidindi, *ACS Appl. Nano Mater.*, 2023, **6**, 238–247.

135  M. Guo, N. Luo, Y. Bai, Z. Xue, Q. Hu and J. Xu, *Sens. Actuators, B*, 2024, **398**, 134151.

136  L. Zhang, J. Xiong, B. Ding, C. Fan, G. Liu and H. Li, *Sens. Actuators, B Chem*, 2024, **407**, 135471.

137  Y. Kumar, I. Ahmad, A. Rawat, R. K. Pandey, P. Mohanty and R. Pandey, *ACS Appl. Mater. Interfaces*, 2024, **16**, 11605–11616.

138  S. Ruidas, L. Pradhan, B. Mohanty, S. Dalapati, S. Kumar, B. K. Jena and A. Bhaumik, *ACS Appl. Energy Mater.*, 2024, **7**, 2872–2880.

139  W. Huang, W. Zhang, S. Yang, L. Wang and G. Yu, *Small*, 2024, **20**, 2308019.

140  Y. Yusran, H. Li, X. Guan, Q. Fang and S. Qiu, *EnergyChem*, 2020, **2**, 100035.

141  Z. Alsudairy, N. Brown, A. Campbell, A. Ambus, B. Brown, K. Smith-Petty and X. Li, *Mater. Chem. Front.*, 2023, **7**, 3298–3331.

142  S. Zhang, D. Liu and G. Wang, *Molecules*, 2022, **27**, 2586–2630.

143  A. Mei, Z. Yang, M. Zhou, W. Jin, Y. Liu and W. Chen, *Anal. Sens.*, 2024, **4**, e202300078.

144  M. Zhou, Y. Li and G. Xu, *TrAC Trends Anal. Chem.*, 2024, **174**, 117679.

145  Y. Shi, L. Ni, Z. Wang, M. Chen and L. Feng, *Coord. Chem. Rev.*, 2024, **505**, 215691.

146  Z. Wang, Y. Li, P. Liu, Q. Qi, F. Zhang, G. Lu, X. Zhao and X. Huang, *Nanoscale*, 2019, **11**, 5330–5335.

147  Y. Tao, W. Ji, X. Ding and B. H. Han, *J. Mater. Chem. A*, 2021, **9**, 7336–7365.

148  B. J. Smith, L. R. Parent, A. C. Overholts, P. A. Beaucage, R. P. Bisbey, A. D. Chavez, N. Hwang, C. Park, A. M. Evans, N. C. Gianneschi and W. R. Dichtel, *ACS Cent. Sci.*, 2017, **3**, 58–65.

149  S. Wang, Q. Wang, P. Shao, Y. Han, X. Gao, L. Ma, S. Yuan, X. Ma, J. Zhou, X. Feng and B. Wang, *J. Am. Chem. Soc.*, 2017, **139**, 4258–4261.

150  H. Duan, K. Li, M. Xie, J. Chen, H. Zhou, X. Wu, G. Ning, A. I. Cooper and D. Li, *J. Am. Chem. Soc.*, 2021, **143**, 19446–19453.

151  Y. Yusran, H. Li, X. Guan, D. Li, L. Tang, M. Xue, Z. Zhuang, Y. Yan, V. Valtchev, S. Qiu and Q. Fang, *Adv. Mater.*, 2020, **32**, 1–9.

152  N. Thokala, K. Vankayala, A. D. Gaonkar, G. Periyasamy, K. Fazl-Ur-Rahman, K. Valle, M. E. Dmello, K. Basavaiah and S. B. Kalidindi, *Sens. Diagn.*, 2023, **2**, 1176–1180.

153  D. W. Burke, C. Sun, I. Castano, N. C. Flanders, A. M. Evans, E. Vitaku, D. C. McLeod, R. H. Lambeth, L. X. Chen, N. C. Gianneschi and W. R. Dichtel, *Angew. Chem., Int. Ed.*, 2020, **59**, 5165–5171.

154  V. Krishnaveni, M. E. Dmello, N. Thokala, A. Bonda, V. K. Sriramadasu, S. Akkenapally, S. B. Bubanale, K. Basavaiah, S. Bhattacharyya and S. B. Kalidindi, *ACS Appl. Nano Mater.*, 2024, **7**, 23416–23422.

155  J. Chen, Y. Wang, Y. Yu, J. Wang, J. Liu, H. Ihara and H. Qiu, *Exploration*, 2023, **3**, 20220144.

156  V. Krishnaveni, M. Esclance Dmello, P. Sahoo, N. Thokala, V. R. Bakuru, K. Vankayala, K. Basavaiah and S. B. Kalidindi, *ACS Appl. Nano Mater.*, 2023, **6**, 10960–10966.

157  N. Thokala, K. Vankayala, K. Basavaiah and S. B. Kalidindi, *Int. J. Hydrogen Energy*, 2024, **81**, 270–279.

158  G. Y. Lee, J. Lee, H. T. Vo, S. Kim, H. Lee and T. Park, *Sci. Rep.*, 2017, **7**, 1–10.

159  I. D. Kim, A. Rothschild and H. L. Tuller, *Acta Mater.*, 2013, **61**, 974–1000.

160  Z. Li, S. Yan, Z. Wu, H. Li, J. Wang, W. Shen, Z. Wang and Y. Fu, *Int. J. Hydrogen Energy*, 2018, **43**, 22746–22755.

161  E. Amani, K. Khojier and S. Zoriasatain, *Int. J. Hydrogen Energy*, 2017, **42**, 29620–29628.

162  H. Steinebach, S. Kannan, L. Rieth and F. Solzbacher, *Sens. Actuators, B*, 2010, **151**, 162–168.

163  M. Govindhan, B. Sidhureddy and A. Chen, *ACS Appl. Nano Mater.*, 2018, **1**, 6005–6014.

164  D. P. Volanti, A. A. Felix, M. O. Orlandi, G. Whitfield, D. J. Yang, E. Longo, H. L. Tuller and J. A. Varela, *Adv. Funct. Mater.*, 2013, **23**, 1759–1766.

165  C. Wang, G. Zhou, J. Li, B. Yan and W. Duan, *Phys. Rev. B: Condens. Matter Mater. Phys.*, 2008, **77**, 1–7.

166  O. K. Varghese, D. Gong, M. Paulose, K. G. Ong and C. A. Grimes, *Sens. Actuators, B*, 2003, **93**, 338–344.

167  https://hdl.handle.net/10603/537933.

168  F. Niu, Z. W. Shao, L. M. Tao and Y. Ding, *Sens. Actuators, B*, 2020, **321**, 128513.

169  W. C. Ko, M. S. Kim, Y. J. Kwon, J. Jeong, W. R. Kim, H. Choi, J. K. Park and Y. K. Jeong, *J. Mater. Chem. A*, 2020, **8**, 19246–19253.

170  F. Niu, Z. W. Shao, J. L. Zhu, L. M. Tao and Y. Ding, *J. Mater. Chem. C*, 2021, **9**, 8562–8569.

171  X. Wu, S. Xiong, Y. Gong, Y. Gong, W. Wu, Z. Mao, Q. Liu, S. Hu and X. Long, *Sens. Actuators, B*, 2019, **292**, 32–39.

172  H. Yuan, N. Li, W. Fan, H. Cai and D. Zhao, *Adv. Sci.*, 2022, **9**, 1–27.

173  M. Souto, K. Strutyński, M. Melle-Franco and J. Rocha, *Chem. – Eur. J.*, 2020, **26**, 10912–10935.

174  G. Benedetto and K. A. Mirica, *Acc. Chem. Res.*, 2024, **57**, 2775–2789.

175  M. Ko, L. Mendecki and K. A. Mirica, *Chem. Commun.*, 2018, **54**, 7873–7891.

176  W. Li, Z. Zhu, Q. Chen, J. Li and M. Tu, *Cell Rep. Phys. Sci.*, 2023, **4**, 101679.

177  M. E. Dmello, N. G. Sundaram and S. B. Kalidindi, *Chem. – Eur. J.*, 2018, **24**, 9220–9223.

178  M. Mathew, P. V. Shinde, R. Samal and C. S. Rout, *J. Mater. Sci.*, 2021, **56**, 9575–9604.

179  R. S. Andre, L. A. Mercante, M. H. M. Facure, L. H. C. Mattoso and D. S. Correa, *Appl. Surf. Sci.*, 2019, **473**, 133–140.

180  B. Mohan, R. Kumari, G. Singh, K. Singh, A. J. L. Pombeiro, X. Yang and P. Ren, *Environ. Int.*, 2023, **175**, 107928.

181 C. Liu, J. Wang, J. Wan and C. Yu, *Coord. Chem. Rev.*, 2021, **432**, 213743.

182 S. Cho, C. Park, M. Jeon, J. H. Lee, O. Kwon, S. Seong, J. Kim, I.-D. Kim and H. R. Moon, *Chem. Eng. J.*, 2022, **449**, 137780.

183 K. K. Liu, Z. Meng, Y. Fang and H.-L. Jiang, *eScience.*, 2023, **3**, 100133.

184 M.-S. Yao, P. Wang, Y.-F. Gu, T. Koganezawa, H. Ashitani, Y. Kubota, Z.-M. Wang, Z.-Y. Fan, K.-i. Otake and S. Kitagawa, *Dalton Trans.*, 2021, **50**, 13236–13245.